Indium Arsenide Quantum Dots for Single Photons in the Communications Band

by

Gregory R. Steinbrecher

S.B. Physics and Electrical Engineering, MIT (2012)

Submitted to the Department of Electrical Engineering and Computer Science
in partial fulfillment of the requirements for the degree of

Master of Engineering in Electrical Engineering and Computer Science

at the

MASSACHUSETTS INSTITUTE OF TECHNOLOGY

June 2013

Author .....
Department of Electrical Engineering and Computer Science
May 24, 2013

Certified by .....
Dr. Eric A. Dauler
Associate Technology Officer, MIT Lincoln Laboratory
MIT Lincoln Laboratory Thesis Supervisor

Certified by .....
Jeffrey H. Shapiro
Julius A. Stratton Professor of Electrical Engineering
MIT Thesis Supervisor

Accepted by .....
Dennis M. Freeman
Chairman, Masters of Engineering Thesis Committee

Indium Arsenide Quantum Dots for Single Photons in the Communications Band

by

Gregory R. Steinbrecher

Submitted to the Department of Electrical Engineering and Computer Science
on May 24, 2013, in partial fulfillment of the
requirements for the degree of
Master of Engineering in Electrical Engineering and Computer Science

Abstract

This thesis presents work towards engineering and characterizing epitaxial Indium Arsenide (InAs) quantum dots as single photon sources in the optical communications C-Band (Conventional Band; 1535 nm–1565 nm wavelength). First, the underlying theory of semiconductor quantum dots and the necessary tools from quantum optics are reviewed. Next, a detailed description is given of the experimental system design, along with an overview of the design and implementation process of a cryogenic scanning laser confocal microscope. Then, the quantum dot growth process is presented along with the results of measurements on early quantum dot samples, which suggested that the initial growth process needed to be refined. We present efforts towards improving the growth process and measurements of quantum dot samples resulting from this new process.

MIT Lincoln Laboratory Thesis Supervisor: Dr. Eric A. Dauler
Title: Associate Technology Officer, MIT Lincoln Laboratory

MIT Thesis Supervisor: Jeffrey H. Shapiro
Title: Julius A. Stratton Professor of Electrical Engineering

Acknowledgments

I owe a number of people thanks for their help and support during the past several years. First and foremost, my advisor at Lincoln Laboratory, Eric Dauler, has been amazingly supportive and available to help with almost any problem, while trusting (and pushing) me to handle far more responsibility than I ever expected to during my Masters. It was at his encouragement that my second undergraduate major was in electrical engineering, rather than math, so I could participate in the VI-A Master of Engineering program and continue working on this project; I haven't regretted taking that advice once.

My faculty advisor, Professor Jeffrey Shapiro, has been extremely generous with his time and advice, and with his feedback on the various drafts of this thesis. I was consistently astounded at the level of detail in his comments, while still providing comments on the bigger picture.

I consider myself extremely lucky that all those at MIT Lincoln Laboratory that I have worked with have been friendly, willing to help, and exceedingly competent. In particular, Christine Wang, with whom I collaborated on the quantum dot growth process, was welcoming and accepting of my efforts, input, and endless questions about a project far outside my normal field; I learned a huge amount about OMCVD and epitaxial growth from working with her. Danna Rosenberg, Matt Grein, and Ryan Murphy were always willing to help in lab, providing advice in their respective areas of expertise along the way.

Thank you to my friends for never showing anything but encouragement for the hours I pour into my research, even when they ensure I maintain some work-life balance.

Finally, I owe everything to my parents, who have been both role models and amazingly supportive of my chosen field. Thank you for everything you've done for me.

Contents

List of Figures

Chapter 1

Introduction

At the heart of quantum mechanics – and the root of its name – lies the concept of quantization. Classically, values like mass, electric charge, and energy take on values in an uncountable (i.e., continuous) set, typically the real numbers or the non-negative real numbers. However, it has since been discovered that nature frequently restricts these values to discrete, or partially discrete, sets. Perhaps most notably, electric charge is always quantized to multiples of the elementary charge. Mass[1] is also discretized to integer combinations of the quarks, leptons, and massive bosons found in the Standard Model.

In many cases, mass and charge are held constant throughout a problem or model, so the implications of their restriction to discrete sets may not be immediately obvious. However, quantum theory also predicts (and experiments have verified) that the values dynamical variables, such as energy, take on may also be restricted to discrete sets.

This quantization of energy has numerous interesting and useful implications. For example, the energy levels that an electron in an atom is permitted to occupy are quantized. Accordingly, the set of *differences* between these energies is also discrete. Thus, when an electron decays from a higher energy orbital to a lower one, emitting a photon, the possible energies for that photon are members of a discrete set.

The spectrum of discrete-transition emissions from an atom forms a fingerprint

[1] Rest mass, if we are considering relativistic effects

for that atom – a set of emission energies unique to that atom. This is exploited, for example, by astrophysicists to determine the chemical composition of faraway galactic objects. Similarly, biologists use fluorescent particles with known spectra as tags to track cells, or parts of cells, with particular properties.

In semiconductors, the discrete electronic energy levels of the individual atoms interact with the symmetries of the crystal to produce bands of allowed energies. These bands include one that is nearly completely occupied by electrons (the valence band) and one that is nearly empty (the conduction band), separated by a band gap of prohibited energies. This band gap (along with extra states created by impurities) is the primary feature that allows semiconductors to be fashioned into transistors, which have been the driving force of the computing revolution, and semiconductor lasers, which lie at the core of the transmitters employed in fiber-optic communications.

Prior to the 19th century, there were two competing theories of light, due to Christiaan Huygens and Isaac Newton. Huygens argued that light was a wave and that the propagation of wavefronts could be predicted by imagining a set of point sources along each wavefront. Newton, in contrast, predicted light to be composed of corpuscules – light particles. However, Newton's theory was unable to account for the interference patterns observed by Thomas Young in his famous double-slit experiment, and the wave theory of light was accepted as the canonical theory.

For another hundred years, classical electrodynamics proceeded with the assumption that the electric and magnetic fields (later unified into a single field) could take on amplitudes anywhere in $\mathbb{R}$; that is, the field components were treated as continuous quantities. However, in 1905, Einstein found he was able to explain the photoelectric effect by restricting the energy of light to multiples of $\frac{hc}{\lambda}$ [1], where h is Planck's constant, c is the speed of light in vacuum, and λ is the free space optical wavelength. For this discovery, Einstein was awarded the 1921 Nobel Prize in Physics. The theory that light is composed of packets of energy (the name photons was introduced later) was incorporated by Paul A. M. Dirac [2, 3] and others [4, 5] into quantum theory, and experiments have continued to confirm that this quantization reflects the behavior of light in the real world.

This thesis covers work towards engineering a single photon source, which is a photon gun that produces one and only one photon at its output when it is triggered. These single photon sources are known as on-demand single photon sources, indicating their ability to produce a photon when triggered. Such sources enable us to exploit the quantized nature of light for a variety of purposes. In particular, single photon sources are highly valuable for quantum key distribution (QKD). Whereas the security of classical encryption schemes relies on the computational difficulty of reversing certain operations (e.g. RSA relies on the relative difficulty of factoring large numbers as compared to multiplying them), quantum encryption systems like QKD instead promise security based on the laws of nature [6].

In order to explain how QKD systems work, and why single photon sources are valuable to them, it is first necessary to review the mathematics of the polarization of light.

1.1 Photon Polarization

First, let us compare the classical and quantum theories of polarization. Classically, the electric field complex envelope of a monochromatic plane wave is given by

$$\boldsymbol{E}(\boldsymbol{r}, t) = \hat{\epsilon} E_0 e^{i(\boldsymbol{k}\cdot\boldsymbol{r} - \omega t)}, \tag{1.1}$$

where E_0 is a complex amplitude, ω is the frequency, and $\boldsymbol{k}$ is its propagation vector, satisfying $|\boldsymbol{k}| = \frac{\omega}{c}$. The polarization unit vector $\hat{\epsilon}$ lies in a plane orthogonal to the axis of propagation, which lies along $\boldsymbol{k}$. For instance, if we take the axis of propagation to be the z-axis, then $\hat{\epsilon}$ lies in the xy-plane.

We may decompose $\hat{\epsilon}$ into its orthogonal projections $\alpha\hat{x} + \beta\hat{y}$ where $|\alpha|^2 + |\beta|^2 = 1$, where, we allow α and β to be complex, corresponding to a phase difference between the $\hat{x}$ projection and the $\hat{y}$ projection of the field. In other words, $\hat{\epsilon}$ may be any unit vector in the two-dimensional vector space $\mathbb{C}^2$.

From the perspective of quantum theory, a photon is a spin-1 particle, meaning

its intrinsic spin angular momentum takes on values in the set $\{-1, 1\}$. However, in order to measure this intrinsic spin in the real world, we must make the measurement with respect to a specific spatial axis. If a non-annihilative measurement shows the spin of a photon to be along, say, the x-axis, we know that it does not have any component along the y-axis. However, after making this measurement, we have *no* information suggesting the outcome of a subsequent measurement along the $\pm 45^\circ$ axes.

The state of the spin is, then, represented by a vector in 2-space, where the basis may be identified with any pair of orthogonal spatial directions. As the rules of quantum theory require that we admit complex superpositions [7], we are again left with a vector in $\mathbb{C}^2$. To distinguish it from other types of vectors, components of this space are usually referred to as 2-spinors.

In summary, the polarization of coherent classical light, and the intrinsic spin of a photon in quantum theory, occupy precisely the same state space, $\mathbb{C}^2$. It has been experimentally verified that this is not merely a coincidence; the polarization of classical light is encoded on each photon individually as its intrinsic spin. As such, we may apply a useful tool from classical optics to our discussion of photons: the Jones calculus.

1.1.1 The Jones Calculus

In classical coherent optics, it is often convenient to work only with the polarization and amplitude of light, rather than the full electric field $\boldsymbol{E}(\boldsymbol{r}, t)$. To do so, it is necessary to pick a basis for the representation. Canonically, the two basis vectors selected are the horizontal and vertical unit vectors, denoted $|H\rangle$ and $|V\rangle$ respectively. In explicit form,

$$|H\rangle = \begin{pmatrix} 1 \\ 0 \end{pmatrix} \text{ and } |V\rangle = \begin{pmatrix} 0 \\ 1 \end{pmatrix}. \tag{1.2}$$

As $\mathbb{C}^2$ is a vector space, we may form new pairs of basis vectors by any superposition $\alpha\,|H\rangle + \beta\,|V\rangle$ where $\alpha, \beta \in \mathbb{C}$ and $|\alpha|^2 + |\beta|^2 = 1$. Two other basis pairs will be

particularly important to our understanding QKD. The first is the basis of diagonal and anti-diagonal polarizations, corresponding to polarizations along +45° and -45° respectively, given by

$$|D\rangle = \frac{1}{\sqrt{2}}(|H\rangle + |V\rangle) = \frac{1}{\sqrt{2}} \begin{pmatrix} 1 \\ 1 \end{pmatrix} \tag{1.3}$$

$$|A\rangle = \frac{1}{\sqrt{2}}(|H\rangle - |V\rangle) = \frac{1}{\sqrt{2}} \begin{pmatrix} 1 \\ -1 \end{pmatrix}. \tag{1.4}$$

The second is the basis formed by the left-hand and right-hand circular polarizations:

$$|L\rangle = \frac{1}{\sqrt{2}}(|H\rangle + i\,|V\rangle) = \frac{1}{\sqrt{2}} \begin{pmatrix} 1 \\ i \end{pmatrix} \tag{1.5}$$

$$|R\rangle = \frac{1}{\sqrt{2}}(|H\rangle - i\,|V\rangle) = \frac{1}{\sqrt{2}} \begin{pmatrix} 1 \\ -i \end{pmatrix}. \tag{1.6}$$

These two bases are special because the magnitude of the projection of $|H\rangle$ is identical to the magnitude of the projection of $|V\rangle$ in each. In fact, this property holds pairwise between all three bases, with both basis vectors of one basis having equal magnitude when projected into either of the other two.

Polarizers

In the Jones calculus, it is straightforward to represent a number of common experimental tools as 2×2 matrices. For instance, the action of a linear polarizer aligned with the x-axis is given by

$$LP\{|H\rangle\} = \begin{pmatrix} 1 & 0 \\ 0 & 0 \end{pmatrix}. \tag{1.7}$$

More generally, a polarizer tuned to select for any polarization $\alpha\,|H\rangle + \beta\,|V\rangle$ is given by the projection matrix onto that polarization. The matrix can be explicitly constructed as the outer product of $\alpha\,|H\rangle + \beta\,|V\rangle$ with itself. For instance, the action of a left-hand

circular polarizer is

$$LP\{|L\rangle\} = |L\rangle\langle L| = \frac{1}{2}\begin{pmatrix}1\\ i\end{pmatrix}\begin{pmatrix}1 & -i\end{pmatrix} = \frac{1}{2}\begin{pmatrix}1 & -i\\ i & 1\end{pmatrix} \tag{1.8}$$

where $\langle\cdot|$ is the dual (here, conjugate transpose) of $|\cdot\rangle$.

1.1.2 Interpretation of Amplitudes

While the classical and quantum cases above may have identical mathematical models, the interpretation of the numerical results is critical. For instance, consider the action of the $LP\{|H\rangle\}$ polarizer on $|\psi\rangle = E_0|D\rangle$:

$$\begin{pmatrix}1 & 0\\ 0 & 0\end{pmatrix}|\psi\rangle = \frac{E_0}{\sqrt{2}}\begin{pmatrix}1 & 0\\ 0 & 0\end{pmatrix}\begin{pmatrix}1\\ 1\end{pmatrix} = \frac{E_0}{\sqrt{2}}\begin{pmatrix}1\\ 0\end{pmatrix} = \frac{E_0}{\sqrt{2}}|H\rangle\,. \tag{1.9}$$

We are left with a state parallel to $|H\rangle$, as we should be, and the amplitude E_0 has been scaled by a factor of $\frac{1}{\sqrt{2}}$. Classically, this corresponds to a scaling of the electric field amplitude by that same factor. Equivalently, the outgoing $|H\rangle$-polarized light only has half of the intensity of the incoming $|D\rangle$-polarized light.

However, photons are quantized – it does not make any sense to discuss half a photon. Instead, according to the rules of quantum theory, the probability of a given state arising is given by the squared norm of the state. Squaring the factor of $\frac{1}{\sqrt{2}}$, we find that there is a $\frac{1}{2}$ probability that we measure a $|D\rangle$-polarized photon to pass through a linear polarizer aligned with $|H\rangle$.

Note that we are assuming that the notion of a photon – a quantum of light – is on some level a familiar concept. Accordingly, we are being slightly imprecise here, using a kind of billiard-ball picture where a photon does or does not pass through a polarizer. This is done in order to motivate the larger picture before diving too deeply into the mathematics. The mathematics and subtleties of the quantum theory are explained in significantly more detail in Chapter 2.

It is always a good idea to confirm that a result from quantum theory yields the

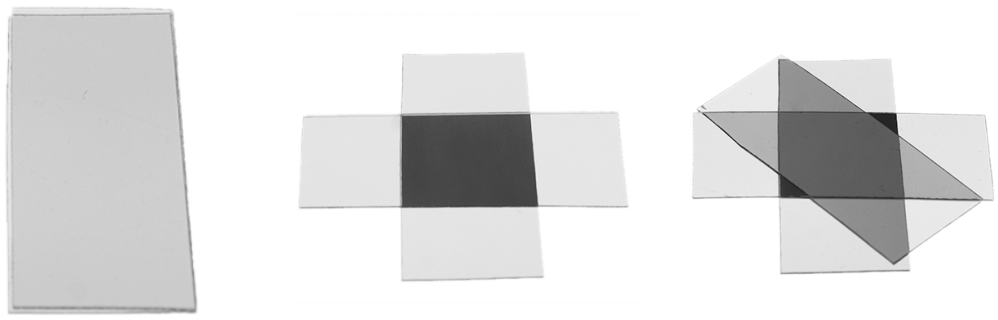

(a) (b) (c)

Figure 1-1: Illustration of a destructive measurement. Shown are polarizers, back lit by a light table. Two polarizers, when aligned parallel as in (a), allow light to be transmitted. Aligned orthogonally, as in (b), they do not allow light to pass where they overlap. However, when a third polarizer is inserted at 45°, as in (c), light passes through all three polarizers, illustrating that the 45° polarizer does not merely select half the photons to transmit, but effects a physical change to their polarization state.

correct result in the classical limit, viz. the many-photon limit. The energy of a photon is determined completely by its wavelength: $E = \frac{hc}{\lambda}$. As intensity of light is measured in units of energy per unit time, we may regard it as the expected, or average, number of photons per unit time. Thus, a classical 50 percent reduction in intensity corresponds to a 50 percent reduction in then number of expected photons per unit time. In the quantum case above, we calculated a one-half probability of any given photon being transmitted, so this matches perfectly.

The most relevant feature of the above example is that the output state from the polarizer is not simply a rescaling of the input state. Instead, the polarization of the output state lies parallel to the polarizer's axis of selection. The consequences of this become clear if we consider the effect of changing the input polarization to lie parallel to $|A\rangle$. The projection onto $|H\rangle$ again yields a factor of $\frac{1}{\sqrt{2}}$ and the output state is necessarily parallel to $|H\rangle$. In other words, the output state is again $\frac{1}{\sqrt{2}}|H\rangle$, completely identical to before. In fact, if we assume the input state is either $|D\rangle$ or $|A\rangle$, the output state contains *no* information about which one it was.

Figure 1-1 demonstrates this physically. In Figure 1-1a, we see two back-lit polarizers with their axes of selection parallel; light passes through both as expected. In Figure 1-1b, the top polarizer is rotated 90°, and light cannot propagate through

both. Light can still be seen where the two do not overlap. Finally, in Figure 1-1c, a third polarizer is inserted between the other two, at a 45° angle to both. As discussed above, this polarizer does not simply select half the light that passed through the bottom (vertical) polarizer; it *modifies* it so that it is able to further pass through the top (horizontal) polarizer. Completely blocked regions are still visible in the corners where the light does not pass through the 45° polarizer.

Classically, if we do not know the polarization state of a wave, we may simply split the beam with a non-polarizing beam-splitter, make multiple measurements, and determine the overall polarization. However, if we have only a single photon, we must *choose* a basis in which to measure the polarization. If we choose the wrong one, the result of our measurement will be statistically independent from the prior state of the photon.

A final important principle is the quantum no-cloning theorem. The theorem states that, given an unknown quantum state, it is impossible to clone that state perfectly [7]. Thus, we cannot simply duplicate a photon with an unknown polarization and measure it many times to determine its state.

The no-cloning theorem is the driving principle behind quantum key distribution: it provides the ability to prepare a state that cannot be measured more than once, and whose information is destroyed if it is measured in the wrong basis.

1.2 Quantum Key Distribution

We construct our communications scenario with the canonical actors: Alice has some message, encoded in binary, that she would like to send to Bob. However, an adversarial actor, Eve, would like to listen to the message Alice is sending Bob, and is assumed to have full access to the communications channel.

In the most common QKD protocol, BB84 [6, 8], Alice generates a set of random 1's and 0's, and transmits these as single photons polarized in either the $\{|H\rangle, |V\rangle\}$ basis or the $\{|D\rangle, |A\rangle\}$ basis. She makes the selection of basis randomly for each bit, not telling Bob which of the two she picked. With no *a priori* information about each

photon's polarization, Bob must select his basis of measurement randomly as well. Assuming perfect preparation, measurement, and channel performance, we expect Bob will make a meaningful measurement on half of the photons Alice transmits.

Over a classical communications channel, which we assume Eve may listen to with impunity, but cannot modify, Bob tells Alice which bases of measurement he selected for each photon. Alice can inform him which of those were correct selections. Then they both throw away the bits for which Bob made the wrong selection, because those bits have no mutual information as the outcomes of Bob's measurements are statistically independent of Alice's transmissions. At this point, Alice and Bob have constructed what is known as a one-time pad (OTP) which, if securely prepared, is the only completely secure form of encryption.

The OTP is used in the following way: Alice adds her message to the OTP modulo 2, generating an encrypted message. She then transmits this ciphertext to Bob over the insecure classical channel and, when Bob performs the same addition with the OTP modulo 2, he is left with the original message. However, without the OTP, the message is simply random 0's and 1's, and Eve can extract no information from it.

Up to now, we have assumed that Eve makes no measurements on the original photons Alice sends to generate the OTP. What if she does?

Again, Alice does not broadcast which basis she is selecting. Thus, Eve must play the same game that Bob does, guessing the basis each time. Half of the bits are thrown away because Bob makes the wrong measurement, so anything Eve does to those photons is irrelevant. Of the measurements Bob makes in the correct basis, Eve will also select the correct basis one-half of the time. However, for the other half, Eve will make the wrong measurement and even though Bob chooses the correct basis, the measurement he makes is statistically independent of the state that Alice prepared; the resulting bit will be different than Alice's one-half of the time. As a result, when Bob performs his addition modulo 2 with his OTP, we expect 25% of the bits to be different than the original message Alice sent.

This is where the security of the QKD scheme lies: Alice and Bob can detect, by the spiking error rate, that someone is eavesdropping on the channel. The laws of

physics, as described above, guarantee that Eve may not listen to the construction of the OTP without irrevocably modifying the process. Thus, communications that are conducted successfully can be verified to have been secure.

It is important to note here that the above discussion assumes Alice and Bob have perfect devices, a perfect communications channel, etc. In fact, these things do not exist in the real world, and determination of a QKD system's security requires significantly more involved analysis. For instance, several systems that were originally thought to be secure have been demonstrated to have classical side-channel attacks [9, 10, 11].

1.3 Sources of Single Photons

Clearly, in order for the above scheme to proceed as described, Alice needs to be able to deterministically produce single photons with known polarization on demand. The aim of the work presented in this thesis is progress towards such a source. As listed in Section 1.3.1, these sources have a number of other potential applications; QKD is provided here as an illustrative example.

Specifically, this work is focused on a single photon source in the optical communications C-Band (Conventional Band; 1535 nm–1565 nm wavelength). Existing fiber-optic networks perform best in the C-Band, and there is accordingly a plethora of high quality equipment developed and optimized for these wavelengths. This includes filters, delay-lines, and (essential to this research) single photon detectors.

In order to answer the question of how to produce single photons, we first need a more specific set of requirements. As discussed in the previous section, QKD relies on Alice's ability to transmit one, and only one, photon in a known polarization state. The photon statistics of a classical light source, as measured on a photon counting detector, typically obey Poisson statistics, with the mean photon number corresponding to the intensity of the light. States of this type are unsuitable for BB84 QKD without some modifications to the described protocol. These are needed because, in the event that more than one photon is transmitted, Eve may pick one

photon off, hold it in a quantum memory until Alice and Bob reveal their basis choices, and make her own measurement in the proper basis without creating errors that Alice and Bob can detect. This would result in information leakage, degrading the security of QKD.

Thus, while it would be tempting to, for instance, take a laser that produces 100 photons per pulse, attenuate it with a 1% transmission filter, and call that a single photon source, such a system would be unsuitable for the types of applications we are interested in without a method to ward off multiple photon attacks by Eve. That is, when we refer to a single photon source, we are not simply making a statement about the mean photon number, we are making a statement about higher statistical moments as well.

The state of light we are interested in producing is a purely quantum state of light known as a number state. Quantum mechanics as a whole is intimately entwined with the ideas of observation and measurement, and quantum optics is no exception. The most important operator for our discussion is the number operator $\hat{N}$, whose eigenvalues correspond to the outcomes of photon-number resolving measurements. That is, the spectrum of $\hat{N}$ is $\mathbb{Z}^+$, the set of all non-negative integers. We define the number state with n photons to be the eigenstate of $\hat{N}$ whose eigenvalue is n. It follows that, for a single photon source, we would like the output state of light to be $|1\rangle$.

Of course, in the real world, sources of single photons are hardly ideal. They do not, for instance, have perfect efficiency, so they will not always produce a photon when Alice requests one. The figures of merit for characterizing a single photon source are:

- η_{total}, the total quantum efficiency of the source. That is, the probability that a photon is produced at the output when the source is triggered.

- $\Delta\lambda$, the uncertainty in the wavelength of the produced photons.

- f_{max}, the maximum frequency with which a source may be triggered.

- $g^{(2)}(0)$, a second-order autocorrelation function measuring the probability that the source produces two photons simultaneously vs. the probability that it produces two photons successively. This statistic is discussed in detail in Section 2.3.

- $F(\Delta t = 0)$, a measure of the degree to which successive photons from a source are quantum mechanically identical.

1.3.1 Other Applications of Single Photon Sources

QKD is merely one possible application of on-demand single photon sources. Others include:

- Two-photon interference applications such as generation of EPR-Bell pairs by combining two indistinguishable photons of orthogonal polarization at a non-polarizing beam-splitter [12, 13, 14, 15].

- A Knill-Laflamme-Milburn controlled-sign quantum gate through single mode teleportation [15].

- Use in proposed quantum-repeaters for generic quantum-optical communications protocols [6, 8, 15].

- Quantum computation of permanents using only linear optics [16].

1.3.2 Single Photon Source Material Systems

Essentially all demonstrated on-demand sources of single photons rely on the same physical principle: a dipole transition in a two-level quantum system. In other words, a charged particle, usually an electron, decays from a high-energy state to a low-energy state through an interaction with the radiation field. As the electron does not occupy any intermediary states (typically, there are no such states, or transition into them is suppressed), the energy must be released in a single excitation of the

field, resulting in a single photon whose wavelength is equal to $\frac{hc}{\Delta E}$ where ΔE is the difference in energy between the two levels.

Of course, systems in the real world are somewhat more complicated than this idealized model. They are at non-zero temperature, there are other fields with which the electron can interact, there are other states it can transition to, there may be a degeneracy of one of the electronic levels, etc. But these are implementation-dependent issues, and a complete discussion can be left until later. For now, we examine candidate material systems.

There are several physical systems that have been demonstrated as sources of single photons:

- Self-assembled semiconductor quantum dots (the system used in the research for this thesis).
- Colloidal quantum dots, also known as nanocrystals.
- Nitrogen vacancy centers in diamond, also known as color centers.
- Semiconductor donors and acceptors.
- Single trapped ions.
- Single molecules.

This thesis covers research on the use of self-assembled semiconductor quantum dots, specifically those composed of Indium Arsenide (InAs) grown epitaxially on a material lattice-matched to InP. The InP lattice spacing is critical to ensure the correct resulting dot size and strain profiles for fluorescence near 1550 nm. These were selected as they show the greatest promise for a single photon source in the C-Band. With the exception of colloidal quantum dots, the other sources have not been demonstrated to perform well in this band. Colloidal dots have their own problems; specifically, they are subject to telegraph noise (also known as blinking), in which they stochastically lose and regain their ability to produce single photons on the timescale of milliseconds [17].

Self-assembled quantum dots, on the other hand, can be tuned over a broad wavelength range by careful selection of material system and growth parameters, are extremely stable over time, and have been successfully demonstrated as sources of single photons at shorter wavelengths. Most notably, InAs quantum dots grown on Gallium Arsenide (GaAs) have been the subject of considerable research as single photon sources in the 980 nm band [13, 14, 18].

Several groups have reported success using InAs dots grown on InP as single photon sources in the C-Band [19, 20], and even performed QKD experiments [21] using such sources. The research reported in this thesis seeks to replicate these successes so that we may employ these sources in novel applications. Further, while initial results of these dots' spectra and photon statistics have been reported, there is still a lot of work to be done in characterizing their electronic states, forming a consistent model of their behavior, improving their performance, and integrating them into systems.

1.3.3 Self-Assembling Quantum Dots

The growth process of self-assembled quantum dots is an essential component of this thesis work. Known as Stranski-Krastanov growth, the process relies on the compressive strain that results from epitaxial growth of a crystal with a larger lattice constant (but the same crystal structure) as that of the substrate. In this work, we grow InAs, which has a lattice constant of 6.0583 Å on an Indium Phosphide (InP) substrate, which has a lattice constant of 5.8687 Å. The epitaxy process used was organometallic vapor phase epitaxy (OMVPE).

During OMVPE growth, In and As atoms adsorb to the surface of the wafer, producing monolayer-by-monolayer growth of InAs. Once the InAs layer reaches a certain thickness, known as the critical thickness, the compressive strain from the lattice mismatch makes it thermodynamically favorable for the InAs to relax into islands, rather than remaining a homogeneous pseudomorphic layer [22]. These islands range from 2 nm to 10 nm in height, and 30 nm to 60 nm in diameter. In general, they are oblong, and can be thought of more like quantum pancakes than the image of

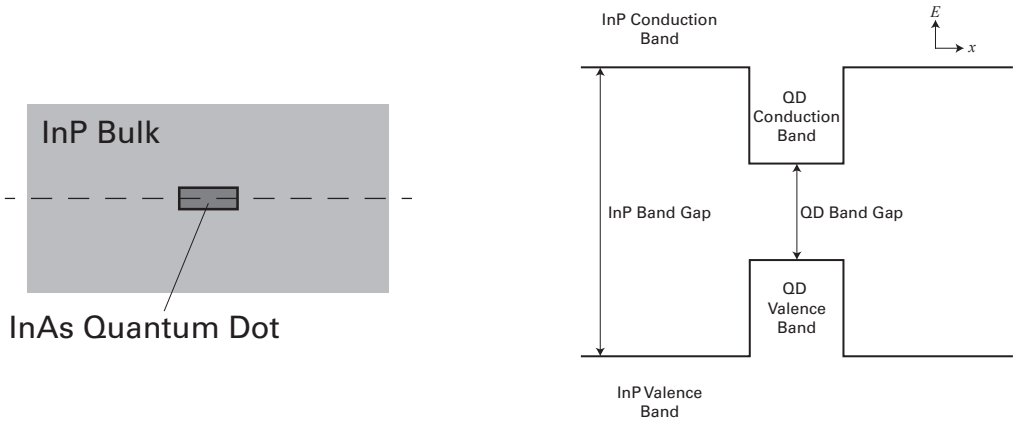

(a) Spatial diagram (b) Energy along dotted line in (a)

Figure 1-2: Idealized illustration of the quantum dot and InP bulk system. (a) shows a simple diagram, with the dotted line indicating the slice along which the energy diagram in (b) is considered. (b) illustrates the existence of allowed energies inside the quantum dot that are inside the band gap of InP. States with these energies cannot exist in the bulk InP, so their wavefunctions are spatially confined to the quantum dot. Note that the actual energy diagram is far more complex due to the effects of strain.

symmetric spheres that the name quantum dots evokes.

The short vertical dimension provides strong electronic confinement, giving rise to a discrete spectrum of excited states that electrons can occupy. Due to the fermionic nature of electrons, only a single electron can occupy any of these states. InAs has a smaller band gap than InP, and their bands align such that the highest energy valence-band state of InAs is higher than that of InP. As such, electronic states near the valence and conduction band edges of InAs are spatially localized to the InAs dot, as electrons of those energies lie in the band gap of InP and are thus excluded from the surrounding InP bulk. An idealized diagram of this energy structure is shown in Figure 1-2.

We create single photons by exciting a large number of electrons in the bulk of the material. As the excited electrons relax through interactions with the phonon fields of the crystal, they inevitably occupy the states localized to the quantum dot. The fermionic exclusion means that only one electron may occupy the lowest-energy excited state. By conservation of energy, a photon that is released from a single dipole

transition has the same energy as the difference between the two energy levels of the transition. As such, we can use a monochromator to select only those photons with the energy (wavelength) matching that of the lowest energy transition. Because there was only one electron in that state, and the transition must occur in a single step, only a single photon will make it through our wavelength filter. By exciting a large number of electrons per trigger pulse, we may assume with moderate probability that one of these transitions occurs with every pulse.

1.4 Discussion

In the rest of this thesis, I review my efforts to engineer a single photon source based on self-assembled quantum dots.

Chapter 2 covers the theory of quantum dots, and how they can be used to produce single photons. The quantum theory of light as it pertains to single photon sources is reviewed as well, with a more detailed discussion of the figures of merit introduced earlier, in Section 1.3

Chapter 3 discusses the experimental design in detail. The first half of the chapter discusses the overall design of the experiment and describes in detail the various components and their interactions. The second half is dedicated to the design and implementation of a cryogenic scanning confocal microscope, a major part of this thesis work.

Chapter 4 covers the organometallic vapor phase epitaxy (OMVPE) process used to grow the self assembled quantum dots developed in this work. Results from early quantum dot growth experiments, acquired using the confocal microscope, are presented, which suggest the need for an improved growth process. The improvements made to this process are discussed, and initial spectrographic results are presented.

Finally, Chapter 5 presents conclusions and avenues for future progress.

Chapter 2

Theory of Quantum Dots and Quantum Optics

Quantum dots are material systems capable of confining electrons in three dimensions. They are analogous to quantum wires, which confine electrons in two dimensions, and quantum wells, which confine electrons in one. This three dimensional confinement – in contrast to the confinement seen in wells and wires – results in a discrete set of energy levels for electrons to occupy, similar to those found in an atom. However, unlike an atom, the values of these energy levels can be tuned by varying the material composition and growth parameters used to produce the quantum dots.

The process used to grow the InAs quantum dots for this thesis is covered in detail in Chapter 4. For now, we focus on the underlying theory with a particular emphasis on the origin of bound states and a discrete energy spectrum. The latter part of this chapter then covers how these systems may be used as the essential component of single photon sources.

2.1 Useful Quantum Toy Models

Directly solving Schrödinger's equation for quantum dots – even relatively small ones – is an intractable problem [23]. They are composed of too many nuclei and electrons; calculating all of the necessary interactions directly would require orders of magnitude

more computing power than the entire world has to offer. Instead, we study small systems, or toy models, that give rise to dynamics and properties similar to those we see in quantum dots.

We first review the theory of two canonical systems: the infinite square well and the quantum harmonic oscillator (hereafter, QHO). Our focus is the origin and spectrum of bound states in these systems, which derive from the spatial confinement of quantum wavefunctions. References for this material may be found in any standard quantum mechanics text [7, 24].

2.1.1 The Infinite Square Well

The most simple model with which to begin a discussion of bound states is one familiar to any quantum mechanics student: the infinite square well. In fact, viewed from a slightly more abstract perspective, it is a system ubiquitous in science and engineering; a student of electrical engineering studies it as a perfectly conducting cavity, a student of acoustics sees it as a resonator with no ports, and equivalent systems are found wherever there are resonances.

We begin by assuming that an electron of mass m_e is subject to a one-dimensional potential $V(x)$ given by

$$V(x) = \begin{cases} 0 & \text{if } |x| < \frac{L}{2} \\ \infty & \text{else.} \end{cases} \tag{2.1}$$

Plugging this into the time-independent Schrödinger equation $\hat{H}\,|\psi\rangle = E\,|\psi\rangle$ yields

$$\left(-\frac{\hbar^2}{2m_e}\frac{\partial^2}{\partial x^2} + V(x)\right)\psi(x) = E\psi(x), \tag{2.2}$$

where we have transitioned from bra-ket notation to a position-space wavefunction $\psi(x)$. Clearly, $\psi(x)$ is subject to Dirichlet boundary conditions at $x = \pm\frac{L}{2}$ and is zero outside $(-\frac{L}{2}, \frac{L}{2})$.

Let us examine the implication of the symmetry $V(-x) = V(x)$. A useful tool

here is the parity operator $\hat{\Pi}$, which maps $x \to -x$. That is, $\hat{\Pi}f(x) = f(-x)$ for any given function f. First, note that $\hat{H}$ commutes with $\hat{\Pi}$ since $\frac{\partial^2}{\partial(-x)^2} = \frac{\partial^2}{\partial x^2}$ and $V(-x) = V(x)$. Next, consider an eigenfunction $\psi(x)$ of $\hat{H}$ such that $\hat{H}\psi(x) = E\psi(x)$. Applying $\hat{\Pi}$ to both sides, $\hat{\Pi}\hat{H}\psi(x) = \hat{\Pi}E\psi(x)$, implying $\hat{H}\left(\hat{\Pi}\psi(x)\right) = E\left(\hat{\Pi}\psi(x)\right)$. This demonstrates that $\hat{\Pi}\psi(x)$ is also an eigenfunction of $\hat{H}$ with the same eigenvalue E. Provided E is a nondegenerate eigenvalue, this means $\psi(x)$ must also be an eigenstate of $\hat{\Pi}$ such that $\hat{\Pi}\psi(x) = \alpha\psi(x)$.

As $\hat{\Pi}$ is a unitary operator, all of its eigenvalues are of magnitude 1. Its spectrum is further restricted by the consideration of $\hat{\Pi}^2$ acting on a state. Clearly, $\hat{\Pi}^2\psi(x) = \alpha^2\psi(x)$. However, $\hat{\Pi}\hat{\Pi}\psi(x) = \hat{\Pi}\psi(-x) = \psi(x)$, so $\alpha^2 = 1$. Combined with the magnitude restriction, we are left with $\alpha = \pm 1$. Thus, eigenfunctions of $\hat{\Pi}$ are either symmetric or antisymmetric with $\psi(-x) = \psi(x)$ or $\psi(-x) = -\psi(x)$ respectively. As we know the eigenfunctions of $\hat{H}$ are also eigenfunctions of $\hat{\Pi}$, the eigenfunctions of $\hat{H}$ must also be symmetric or antisymmetric.

In the region $-\frac{L}{2} < x < \frac{L}{2}$, $\psi(x)$ must be an eigenfunction of the negative Laplacian, meaning it is a harmonic function [25]. Combining this with the restriction of the eigenfunctions to be even or odd, we know each eigenfunction will either be a pure sine function or a pure cosine function. Imposing the boundary conditions $\psi(\pm\frac{L}{2}) = 0$, the wavefunction is given by $\psi_s(x) = A\cos(\frac{(2n-1)\pi x}{L})$ or $\psi_a(x) = B\sin(\frac{2n\pi x}{L})$, where $n \in \{1, 2, ...\}$ and the s and a subscripts denote symmetric and antisymmetric solutions respectively. Since the phase is irrelevant, we set $A = B = \sqrt{\frac{2}{L}}$ for simplicity.

Finally, we compute the eigenvalues to be:

$$E_{s,n} = \frac{\pi^2\hbar^2}{2m_eL^2}(2n-1)^2 \text{ and } E_{a,n} = \frac{\pi^2\hbar^2}{2m_eL^2}(2n)^2 \tag{2.3}$$

where, by relabeling $2n \to n$, we can see that the energies are ordered

$$E_n = \frac{n^2\pi^2\hbar^2}{2m_eL^2} \tag{2.4}$$

with $n \in \{1, 2, ...\}$, odd n corresponding to the energies of symmetric solutions, and even n corresponding to the energies of antisymmetric solutions.

This quantization of energy levels is our primary interest here. If we restrict our view to a one-dimensional world, the electron may only be measured to have one of the above energies. However, we live in a three-dimensional world; when we embed the above one-dimensional potential in a three dimensional coordinate system, Schrödinger's equation becomes

$$\left(-\frac{\hbar^2}{2m_e}\nabla^2 + V(\boldsymbol{r})\right)\psi(\boldsymbol{r}) = E\psi(\boldsymbol{r}). \tag{2.5}$$

Rearranging this yields

$$\left(-\frac{\hbar^2}{2m_e}\nabla^2 + V(\boldsymbol{r}) - E\right)\psi(\boldsymbol{r}) = 0 \tag{2.6}$$

$$\left(\nabla^2 + \frac{2m_e}{\hbar^2}\left[E - V(\boldsymbol{r})\right]\right)\psi(\boldsymbol{r}) = 0 \tag{2.7}$$

where it is clear that this is an instance of the Helmholtz wave equation $(\nabla^2 + k^2)f = 0$ with $k^2 = \frac{2m_e}{\hbar^2}\left[E - V(\boldsymbol{r})\right]$. As the Helmholtz wave equation is separable in Cartesian coordinates [25], so long as $V(\boldsymbol{r})$ is separable as well (i.e., $V(x, y, z) = V_x(x)V_y(y)V_z(z)$ for some V_x, V_y, and V_z), we may take $\psi(\boldsymbol{r}) = \psi_{1\mathrm{D}}(x)\psi_y(y)\psi_z(z)$ where $\psi_{1\mathrm{D}}$ is the 1D solution found in the previous section, and ψ_y and ψ_z are other factors. Despite the only change from the one-dimensional system to this one being the embedding into a three-dimensional space, the resulting dynamics are not the same. Here, $V(\boldsymbol{r}) = V(x)$ and the problem has continuous translational symmetry in the y and z coordinates, meaning the potential energy of the electron is completely impervious to its position in the yz-plane. The result of this is a *lack* of quantization in energy; the wavefunction factors $\psi_y(y)$ and $\psi_z(z)$ may be any functions satisfying $-\partial^2\psi = 0$. Thus, these components of the eigenfunctions of the Hamiltonian are plane waves of any wavenumber and the overall wavefunction may have any energy.

So while a quantum well may provide discrete energy levels in one dimension, when embedded in a three-dimensional coordinate system its energy spectrum becomes continuous. We may, however, extend the confinement to all three dimensions in a straightforward manner by taking the tensor product of three one-dimensional

quantum well systems. That is, set the potential to be

$$V(x,y,z) = \begin{cases} 0 & \text{if } |x| < \frac{L_x}{2} \text{ and } |y| < \frac{L_y}{2} \text{ and } |z| < \frac{L_z}{2}, \\ \infty & \text{else.} \end{cases} \tag{2.8}$$

Again, we may make use of the separability of the wave equation in Cartesian coordinates. Here, this means the solutions are of the form

$$\psi_{n_x,n_y,n_z}(x,y,z) = A\psi_{1D,n_x}(x)\psi_{1D,n_y}(y)\psi_{1D,n_z}(z) \tag{2.9}$$

where each of the factors is the corresponding 1D eigenfunction. Choosing A real, normalization dictates $A = \sqrt{\frac{8}{L_x L_y L_z}}$. Making further use of the separated system, we see that $E = E_x + E_y + E_z$, implying that

$$E = \frac{\pi^2\hbar^2}{2m_e}\left[\left(\frac{n_x}{L_x}\right)^2 + \left(\frac{n_y}{L_y}\right)^2 + \left(\frac{n_z}{L_z}\right)^2\right]. \tag{2.10}$$

By providing a confining potential in all three dimensions, we have returned to a completely discrete energy spectrum, turning the quantum well into a quantum dot.

2.1.2 The Quantum Harmonic Oscillator

The QHO is perhaps the most important potential introduced in quantum mechanics. Not only does it recur in a surprising number of contexts, the methods developed in its study(most notably, raising and lowering operators) have found application in a diversity of fields. In contrast to the previous section, we do not solve Schrödinger's equation directly in this section. Instead, we provide the ground state solution and then introduce operators which allow us to climb the ladder of energy states. This gives, inductively, the full spectrum.

The potential for the one-dimensional quantum harmonic oscillator is given by

$$V(x) = \frac{1}{2}m_e\omega^2 x^2. \tag{2.11}$$

The lowest energy eigenfunction of the Hamiltonian is then given by

$$\psi_0(x) = \sqrt{\frac{2\pi\hbar}{m_e\omega}} e^{\frac{-m_e\omega x^2}{2\hbar}}, \tag{2.12}$$

which has energy eigenvalue $\frac{\hbar\omega}{2}$.

Next, we introduce two operators, $\hat{a}^\dagger$ and $\hat{a}$, which allow us to map an eigenstate of the Hamiltonian to, respectively, the next higher or lower energy eigenstate. These operators are given in position space by

$$\hat{a}^\dagger = \sqrt{\frac{m\omega}{2\hbar}} \left(x - \frac{\hbar}{m_e\omega} \frac{\partial}{\partial x} \right) \text{ and } \hat{a} = \sqrt{\frac{m\omega}{2\hbar}} \left(x + \frac{\hbar}{m_e\omega} \frac{\partial}{\partial x} \right). \tag{2.13}$$

It is straightforward to verify that, if $\hat{H}\psi(x) = E\psi(x)$, $\hat{H}\hat{a}^\dagger\psi(x) = (E + \hbar\omega)\psi(x)$ and that $\hat{H}\hat{a}\psi(x) = (E - \hbar\omega)\psi(x)$ provided $E > \hbar\omega$. That is, $\hat{a}^\dagger\psi(x)$ and $\hat{a}\psi(x)$ are also eigenfunctions of the Hamiltonian, with energies shifted by $\hbar\omega$ in either direction.

We may thus identify a spectrum of energy eigenstates, starting with $\psi_0(x)$ above, whose energies are given by $\hbar\omega(n+\frac{1}{2})$. We demonstrate that these are the only energy eigenstates by noticing that $\hat{H} = \hbar\omega\left(\hat{a}^\dagger\hat{a} + \frac{1}{2}\right)$. Clearly, any energy eigenstate must fall on the spectrum of operators outlined above (which may also be verified to be complete).

Finally, we introduce the number operator $\hat{N} = \hat{a}^\dagger\hat{a}$ which has the same eigenstates as $\hat{H}$, and whose eigenvalue is n when the state's energy is $\hbar\omega(n + \frac{1}{2})$.

These techniques are the foundation of a quantum formulation of the electromagnetic field. Our study will be a purely single-mode one, so $\hat{a}^\dagger$ and $\hat{a}$ will correspond, respectively, to the creation and destruction of a photon in that mode. The number operator introduced above is essential; we are trying to construct a source that will reliably produce an eigenstate of $\hat{N}$ with eigenvalue 1.

For now, however, we turn to the semiconductor physics of quantum dots.

2.2 Semiconductor Quantum Dots

The quantum dots used in this thesis are composed of small regions of a III-V semiconductor, InAs, embedded in a larger bulk III-V semiconductor, InP. Semiconductors by definition have in their ground state a band of completely occupied states, the valence band, and a band of unoccupied higher energy states, the conduction band. These are separated by a band of prohibited energies known as the band gap of the semiconductor.

The required quantum confinement for our small regions of InAs to be quantum dots arises from the fact that InAs has a smaller band gap than InP, meaning that there exist energies for which electrons are permitted in the InAs region, but prohibited in the InP region. As in Figure 1-2, electrons with these energies are confined in all three dimensions to the InAs region, resulting in a confinement of the electron's wavefunction similar to the confinement studied in the previous several sections.

In this section, we briefly review the origin and structure of the energy bands in III-V semiconductors, discuss the effects of strain on this structure, and provide a simple model that exhibits most of the electronic properties of these quantum dots.

2.2.1 III-V Semiconductor Band Structure

The band structure of energy states in a semiconductor crystal is strongly dependent on the underlying symmetry. In particular, the physical structure of crystals breaks the continuous translational symmetry that typically allows for energy eigenstates spaced arbitrarily close together. Instead, this symmetry is replaced by *discrete* translational symmetry where, when the crystal lattice is displaced by one of its lattice vectors, the original lattice is recovered.

In particular, all the III-V semiconductors we consider in this thesis have a zincblende crystal structure. As illustrated in Figure 2-1, this structure is composed of two face-centered cubic (FCC) lattices with lattice constant a offset by $a/4$ from each other. The bonding is tetrahedral, with all four bonds from each atom going to an atom of the other species.

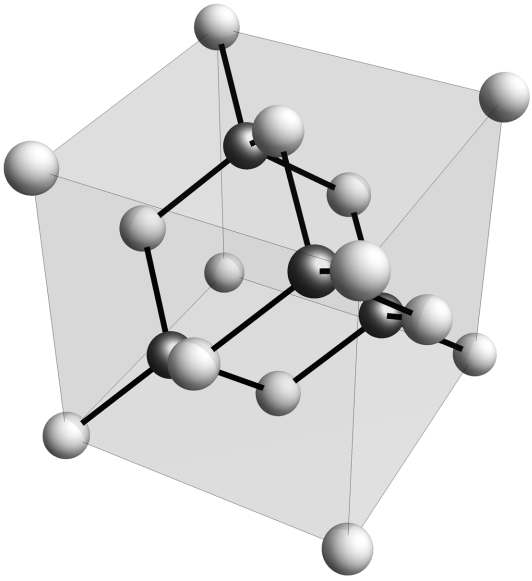

Figure 2-1: Zincblende unit cell. Darker and lighter atoms represent those of the two differing species. Of note is the fact that this structure does *not* have inversion symmetry; reversing one of the axes does not produce the same structure. The thin lines on the edges of the cube represent the boundaries of the unit-cell; they are not bonds.

Clearly, the structure of the crystal lattice will give rise to the structure of the potential an electron feels; the lattice points are the locations of nuclei, each of which has some Coulombic potential associated with it. As such, it is clear that the potential has the same discrete translational symmetry as the crystal; $V(\boldsymbol{r}) = V(\boldsymbol{r} + n_1\boldsymbol{R}_1 + n_2\boldsymbol{R}_2 + n_3\boldsymbol{R}_3)$ where the $\boldsymbol{R}_i$ are the three unit vectors pointing along the axes of the crystal lattice and $n_i \in \mathbb{Z}$.

In a potential with this type of discrete translational symmetry, valid eigenfunctions of the Hamiltonian must obey Bloch's theorem [26]:

$$\psi_{n,\boldsymbol{k}}(\boldsymbol{r}) = e^{i\boldsymbol{k}\cdot\boldsymbol{r}} u_{n,\boldsymbol{k}}(\boldsymbol{r}) \tag{2.14}$$

where $u_{n,\boldsymbol{k}}$ is some periodic function that has the same discrete translational symmetry as the lattice: $u_{n,\boldsymbol{k}}(\boldsymbol{r}) = u_{n,\boldsymbol{k}}(\boldsymbol{r} + n_1\boldsymbol{R}_1 + n_2\boldsymbol{R}_2 + n_3\boldsymbol{R}_3)$. The index n is a label for the band number; there may be several u with the same $\boldsymbol{k}$ but different energies.

The relationship between the wave vector $\boldsymbol{k}$ and the energy $\epsilon_n(\boldsymbol{k})$ is the essential

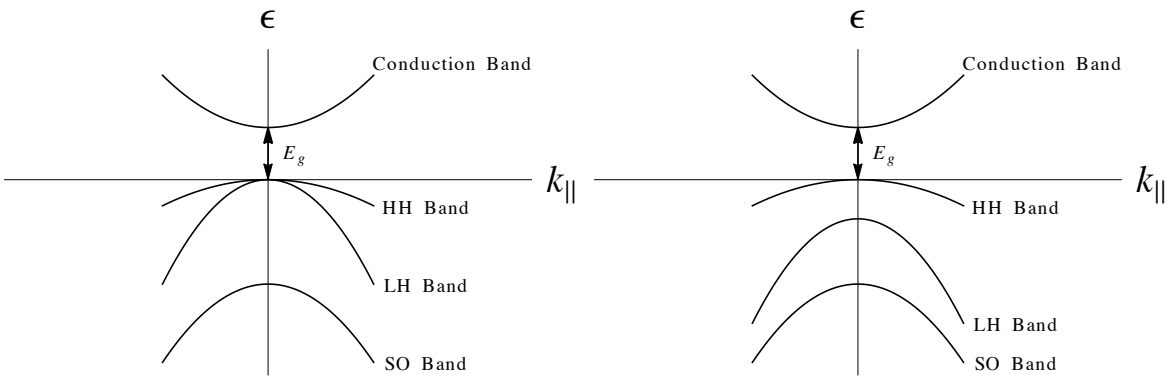

(a) Unstrained (b) Strained

Figure 2-2: Cartoon of dispersion relation for zincblende type semiconductors. Note the splitting between the heavy-hole (HH) and light-hole (LH) bands in (b). $k_{||}$ indicates the wavenumber parallel to the strained axis. SO denotes spin-orbit. Adapted from Reference [27].

relationship in this system, and is known as the dispersion relation. It gives the change in wave vector of a state with respect to changing energy, or vice-versa. Further, if we obtain this relation for all bands, we have a full accounting of the possible energies an electron may take on, and what their wave vector is when they do.

A cartoon picture that captures the major features of this dispersion relation for III-V zincblende semiconductors, expanded around $\boldsymbol{k} = \mathbf{0}$, is included in Figure 2-2a. The most important feature of this picture is the gap in energies near $\boldsymbol{k} = \mathbf{0}$. These are energies that electrons never take on, no matter what band they belong to or what $\boldsymbol{k}$ they have.

Next, note that the valence band is split into three separate sub-bands, the heavy-hole band, the light-hole band, and the spin-orbit split-off band. The spin-orbit split-off band is a function of the relativistic interaction between a charged particle and its angular momentum. It is not of particular interest to us here because we are concerned only with the band edge transitions of electrons. As this is our concern, we wish to ensure there are no degenerate states near the band edge; if there are multiple holes at the same energy, our goal of approximating a simple two-level electronic system gets significantly harder. Described in detail in Chapter 4, the epitaxial growth of our quantum dots involves introducing compressive strain to induce the formation of

the InAs islands. As can be seen in Figure 2-2b, the effect of introducing this strain is to move the light hole band farther away from the band gap in energy, ensuring that there is only one set of states at the band edge, so long as one ignores spin degeneracy.

Electrons are spin-$\frac{1}{2}$ particles and would, in a normal cubic lattice system, have a degeneracy in spin. However, as can be seen in Figure 2-1, the zincblende crystal structure lacks an inversion symmetry; mapping $x \to -x$ does *not* yield the same crystal structure. This breaks the spin degeneracy, ensuring that the electrons have single electronic states to occupy at the band-edge [27].

2.2.2 A Simple Electronic Model

Following [18] and more specifically [28], we may construct a good heuristic model for the band edge spectrum of these quantum dots – that is, those states near the band gap that are confined to the dot – by combining the two toy-model systems discussed earlier. Making the effective mass approximation, the Bloch wave envelope function $f(\boldsymbol{r})$ satisfies [26]

$$\left[-\frac{\hbar^2}{2m^*}\nabla^2 + V(\boldsymbol{r})\right] f(\boldsymbol{r}) = Ef(\boldsymbol{r}) \tag{2.15}$$

where m^* is the effective mass and the potential is harmonic in x and y and an infinite square well in z:

$$V(\boldsymbol{r}) = \begin{cases} \frac{1}{2}m^*\omega^2(x^2+y^2) & \text{if } |z| < L/2 \\ +\infty & \text{if } |z| \geq L/2 \end{cases} \tag{2.16}$$

The reason for this asymmetry is the particular shape of epitaxial quantum dots. Unlike colloidal quantum dots, which are typical spherical or oblong, eptiaxial quantum dots are shaped more like pancakes. Typical dimensions are 30 nm to 50 nm in diameter, lying in the plane of the substrate, and 3 nm to 5 nm tall. The short height is the primary source of the quantum confinement; we represent this here with the infinite square well in z, the direction perpendicular to the substrate.

Note that the potential is the tensor product of three 1D systems, one infinite square well and two quantum harmonic oscillators. Thus, we may solve each dimen-

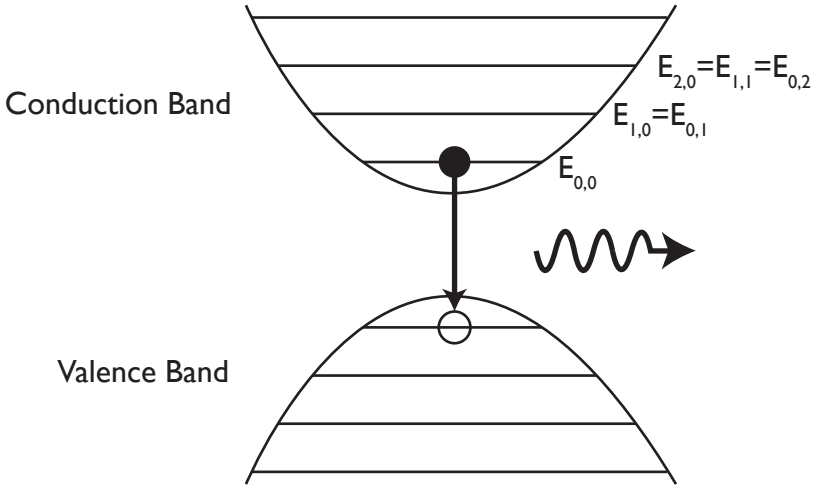

Figure 2-3: Depiction of the energy states of the simple electronic model described in Section 2.2.2. Adapted from [18].

sion separately and add their eigenenergies to get the full eigenenergy spectrum:

$$E = (n_x + n_y + 1)\hbar\omega + \left(\frac{\pi^2\hbar^2}{2m^*L^2}\right) {n_z}^2 \tag{2.17}$$

as is depicted in Figure 2-3. Note that the figure denotes the set of excited electronic states as the conduction band.

InAs dots grown on GaAs generally have an energy spacing of 30-80 meV between the first two electron energy levels [18], which gives an order of magnitude estimate for what we should expect on InP. This is important as the thermal energy of k_bT at 300 K (approximately room temperature) is 25 meV, indicating that to be able to clearly differentiate radiation from a single energy level, we will need to perform measurements at cryogenic temperatures where, for 4 K, k_bT is less than 1 meV.

The final relevant features of the electronic energy spectrum are the spatial symmetries of the excited electron and hole wavefunctions. As discussed in the previous section, the excited electrons have spherical, or s-like, symmetry implying a single set of excited states. However, holes have p-like symmetry, meaning there are three sets of states that can mix. These are typically denoted the heavy-hole, light-hole and split-off bands. It is typical to make the heavy-hole approximation in which, when

the axis of quantization is taken to be the z-axis, the highest valence band state (the lowest energy in which a hole can exist) is a heavy-hole state. The periodic component of the hole wavefunctions are then given by the two states $|m_j = \frac{3}{2}\rangle = |m = 1, \uparrow\rangle$ and $|m_j = -\frac{3}{2}\rangle = |m = -1, \downarrow\rangle$, where m and m_j are the z projections of, respectively, the orbital and total angular momenta [18].

Under this assumption, together with the rotating wave approximation, the dipole moment of the electron-hole recombination yields, in the far field, circularly polarized radiation whose intensity is proportional to $(1 + \cos^2(\phi))$, where ϕ is measured to the z-axis [29]. This implies a circularly polarized photon; in fact, due to the broken inversion symmetry discussed previously, there is a slight energy splitting between the two polarizations or, in other words, a slight splitting between the $m = 1$ and $m = -1$ states. Note that, in the heavy-hole approximation, this also manifests itself as a breaking of the spin-$\frac{1}{2}$ degeneracy.

2.3 Quantum Optics of Single Photon Sources

We need to make precise the notion of a single photon source. This hinges on the idea of a device capable of being triggered to provide a photon gun: when we pull the trigger, we want one and only one photon to be produced at the output a short time later.

From a mathematical perspective, a single photon source should have a low probability of emitting two or more photons per pulse. To make this notion precise, we use the photon correlation function $G^{(2)}(t_1, t_2)$, defined as [12]

$$\left\langle \hat{a}^\dagger(t_1)\hat{a}^\dagger(t_2)\hat{a}(t_1)\hat{a}(t_2) \right\rangle \tag{2.18}$$

where $\hat{a}^\dagger(t)$ and $\hat{a}(t)$ are respectively the photon creation and annihilation operators at time t. This correlation function is typically measured using a beamsplitter to direct the emission from the source to two separate detectors whose output is sent to a circuit that measures coincidences in time. Defining $\hat{a}_1$ and $\hat{a}_2$ to be the annihilation

operators for the two beamsplitter outputs, we may rewrite the above as

$$G^{(2)}(t_1, t_2) = 4 \left\langle \hat{a}_1^\dagger(t_1)\hat{a}_1(t_1)\hat{a}_2^\dagger(t_2)\hat{a}_2(t_2) \right\rangle \tag{2.19}$$

$$= 4 \left\langle \hat{N}_1(t_1)\hat{N}_2(t_2) \right\rangle \tag{2.20}$$

where $\hat{N}_i(t)$ is the photon number operator for output i at time t and the factor of 4 arises from the commutation relation $[\hat{a}, \hat{a}^\dagger] = 1$. Assuming stationary statistics, the normalized correlation function $g^{(2)}(\tau)$ is typically used:

$$g^{(2)}(\tau) = \frac{\left\langle \hat{N}_1(0)\hat{N}_2(\tau) \right\rangle}{\langle \hat{N}_1(0) \rangle \langle \hat{N}_2(0) \rangle}. \tag{2.21}$$

$g^{(2)}(0)$ places an upper bound on the probability of multi-photon emissions by the relation [12, 18]

$$\Pr\{n \geq 2\} \leq \frac{1}{2} g^{(2)}(0) \langle n \rangle^2 \tag{2.22}$$

where n is the number of photons in a given pulse and $\langle n \rangle$ denotes the average number of photons per pulse which, for a single photon source, should be very near 1. Note that for a source with Poisson statistics, $g^{(2)}(0) = 1$, while for an ideal single photon source $g^{(2)}(0) = 0$. If $0 < g^{(2)}(0) < 1$, we say that the source is a sub-Poissonian source. Obviously, an experimentally realized single photon source may have $g^{(2)}(0) << 1$, but it will necessarily be nonzero due to experimental non-idealities. To summarize, the two figures of merit here are $\langle n \rangle$ and $g^{(2)}(0)$ which should respectively be close to 1 and 0 for a near-ideal single photon source.

The details of the experimental design, discussed in the next chapter, allow us to simplify this picture even further. Specifically, the repetition time of the quantum dot stimulation is long enough, and the collection efficiency of the system low enough, that we may mostly neglect the issue of dead-time on the detectors, where a recorded count temporarily decreases the detection efficiency by blocking that channel for a small amount of time. Thus, we can discretize time as well as counts, leading to a

discrete formula for the $g^{(2)}$ calculation [12]:

$$g^{(2)}[j] = \frac{\langle n_1[0] n_2[j] \rangle}{\langle n_1[0] \rangle \langle n_2[0] \rangle} \tag{2.23}$$

where $n_i[j]$ is the number of photons detected by detector i during pulse period j. For our current experimental conditions, this value well approximates $g^{(2)}(0)$.

2.4 Summary

This chapter has covered the theory of quantum dots and quantum optics that is necessary for this thesis. The important quantum mechanical results are an understanding of the effects of strain (splitting of the light and heavy hole bands) and lack of crystal inversion symmetry (spin-degeneracy splitting). Optically, we expect a radiation intensity pattern proportional to $(1 + \cos^2(\phi))$. Finally, we have established the important figure of merit, the discrete $g^{(2)}$ and why $g^{(2)}[0] < 1$ implies a light source with sub-Poissonian statistics.

Chapter 3

Confocal Microscopy: Isolation of Single Quantum Dots

Our main objective in engineering a single photon source is the isolation of a system that well approximates a two-level electronic system. As discussed earlier, the dipole transition of an electron from the excited state to the ground state of such a system is the basis for most on-demand single photon sources. Use of such a system to produce single photons may be separated into two steps: the creation of the excited two-level system (that is, a two-level system with the electron in the higher energy state), and the collection of the resulting dipole radiation.

In this work, we attempt to isolate such a system in a single quantum dot. The aim of doing so is complicated by the density of quantum dots resulting from OMVPE Stranski-Krastanov growth; most of the samples measured had quantum dot densities on the order of 20-100 μm^{-2}. Even with a high numerical aperture (NA) confocal microscope (whose design and implementation is one focus of this chapter), the smallest diffraction-limited spot size achievable is several square microns. As such, we need to work with low density samples (or artificially reduce the density, as discussed later in the chapter) and to rely on the inhomogeneous broadening of the ensemble quantum dot spectrum to separate quantum dots that are simultaneously in view by spectrally filtering out the radiative wavelengths of all but a single dot.

In this chapter, we first provide a detailed overview of the different components of

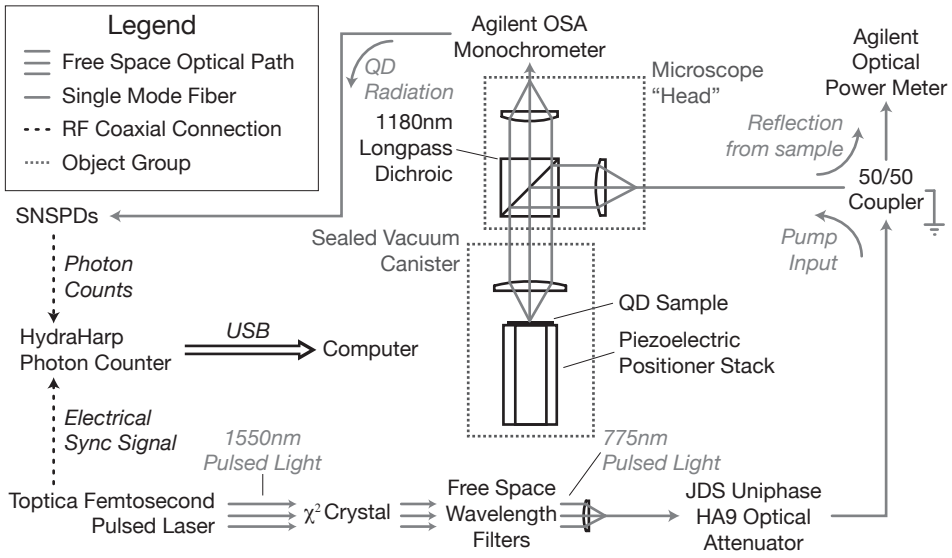

Figure 3-1: Experimental system diagram. With the exception of the HydraHarp ↔ Computer connection, control layer connections are not shown so as to not clutter the diagram.

the system in order to establish the context for the optical design and implementation choices. We then provide a detailed discussion of the theory, implementation, and verification of the confocal microscope that comprised a large portion of this thesis work.

3.1 System Overview

The experimental system designed and built for this work can be broken into three layers: the optical layer, the analog layer, and the control layer. The optical layer is composed of the excitation source, the confocal optics, the quantum dot sample, the spectral filter, and the single photon detectors. This layer interacts with the analog layer at its two ends: the pump laser provides a timing (sync) signal used for time-resolved measurements, and the output radiation of the optical layer is focused onto superconducting nanowire single photon detectors (SNSPDs) that produce an electric pulse for each photon detected. These two electrical signals are brought together at the photon-counting electronics, a PicoQuant HydraHarp 400, which is connected via USB to the computer that manages the control layer. A schematic of the optical

and analog layers is shown in Figure 3-1. Also connected to the control layer are the optical attenuator, the optical spectrum analyzer (OSA) that acts as a fiber-coupled monochromator, the piezoelectric steppers and scanner used to position the quantum dot sample, and the power meter used to monitor the pump-laser reflection.

The rest of this section is dedicated to reviewing the details of all parts of this system with the exception of the confocal microscope, which Section 3.2 is dedicated to describing. The microscope is fiber coupled and only has two connections: the pump fiber port and the collection fiber port which the optical stimulation (Section 3.1.1) and optical filtering (Section 3.1.2) components are connected to respectively.

3.1.1 Optical Stimulation

The band gap of InP at room temperature is 1.35 eV, corresponding to a photon whose wavelength is 918 nm. In order to create carriers in the bulk, the pump laser must produce photons whose energy exceed this band gap (i.e., whose wavelength is shorter than 918 nm). For this purpose, we use a mode-locked fiber laser from Toptica that produces pulses of 1550 nm wavelength light on the order of 100 fs duration at a rate of 100 MHz. As seen along the bottom part of Figure 3-1, the free space output of the laser is then fed to a crystal with a second-order nonlinearity. The crystal is temperature-tuned for phase matching to produce 775 nm up-converted light. Due to the extremely high peak power of the laser, there is also a relevant amount of energy at 517 nm from the third order nonlinearity in optical fiber[1] as well as at 387.5 nm from fourth order conversions in the crystal. Finally, nonlinear up-conversion is not a terribly efficient process; the majority of the optical power following the crystal is still at 1550 nm.

The 1550 nm light is implicitly filtered; it does not propagate in single-mode fiber designed for 780 nm. However, the 517 nm and 387.5 nm light will propagate in a multi-mode fashion in the 780 nm fiber and, if not suppressed, may lead to unwanted stimulation of the samples and/or other uncontrolled behavior. These wavelengths

[1]The Toptica laser itself is a fiber laser; the generation and amplification of pulses occurs entirely in fiber. This fiber is coupled to free space and collimated at the output of the laser.

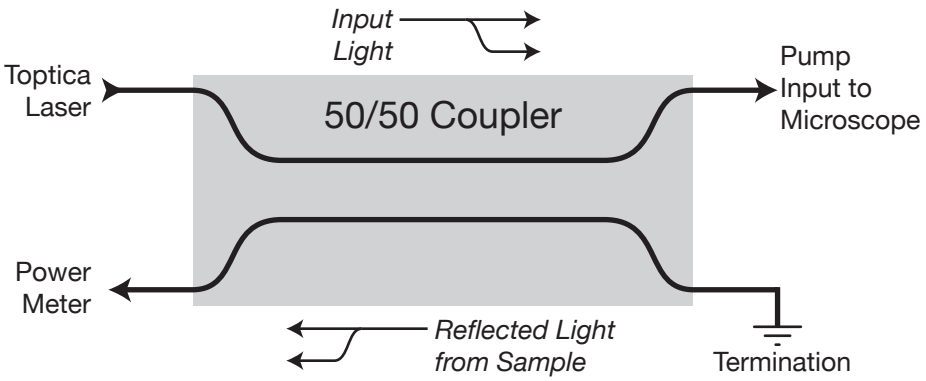

Figure 3-2: Depiction of the use of a 50/50 fused fiber coupler to monitor focus through reflection strength.

are filtered out in free space before the light is coupled into the fiber, allowing the fiber coupling optics to be optimized using a power meter without spurious effects from the other wavelengths.

Once in fiber, we make use of a commercial attenuator, the JDS Uniphase HA9, which may be nominally tuned from 0 dB to 70dB attenuation. In reality, as the HA9 is designed for use at 1550 nm, there is approximately 8 dB insertion loss at 775 nm, making its tunable attenuation range 8 dB to 78 dB. Despite being designed for 1550 nm attenuation, its calibration may be tuned in wavelength; its linearity at 775 nm over the full attenuation range was experimentally confirmed with a power meter.

Like the majority of the equipment used, the HA9 is controlled by the computer via a GPIB interface, which allows for rapid testing of the saturation of the fluorescence at high pump power. Additionally, it allows for observation of power-dependent changes in spectrum when paired with the optical filtering discussed in the next section.

The attenuated output of the HA9 is fed to one input of a 50/50 fused fiber coupler as pictured in Figure 3-2. Of the two outputs, one is terminated with an angled fiber connector to prevent back reflections; the other is fed to the pump input of the microscope. When the laser is in focus on the sample, the index difference between air and InP results in a reflection back into the same mode. This is measured by connecting an optical power meter to the second input to the fused fiber coupler. The reflected power can be used to optimize the pump-laser focus; the reflected power

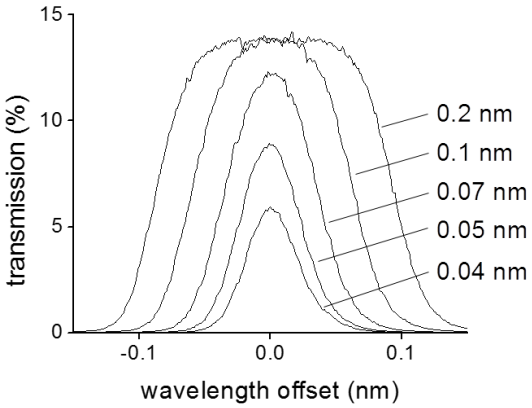

Figure 3-3: Transfer function of the Agilent OSA monochrometer at different bandwidths.

is highest when the pump-laser is in focus.

3.1.2 Optical Filtering

In order to isolate emission from single quantum dots, we need to restrict our view to photons whose energy is in a (tunable) small range. This is accomplished through the use of a monochromator. As our system is fiber coupled, we make use of the monochromator built into our commercial OSA. The center wavelength is tunable over the range 600 nm–1700 nm and the bandwidth is tunable over the range 0.04 nm–10 nm. The insertion loss is on the order of 10 dB, although it varies with bandwidth (increasing for small bandwidths). The measured transfer function at 1550 nm for varying bandwidths is shown in Figure 3-3. The OSA is also connected to the computer via a GPIB interface which allows us to quickly acquire spectra by stepping the center wavelength and measuring the changing count rate of the collected fluorescence.

3.1.3 Microscope Cryostat

At room temperature, the interactions between the electronic states and the phonon fields in the crystal cause too much variation in the energy levels to obtain the isolated excitonic state that we are interested in studying. As such, it is necessary to make

measurements while the sample is kept at cryogenic temperatures, typically between 4.2 Kelvin (the boiling point of liquid helium at 1 atmosphere) and 77 Kelvin (the boiling point of liquid nitrogen at 1 atmosphere). For this work, an existing cryogenic scanning near-field optical microscope from attoCube systems was adapted to support operation as a confocal microscope while preserving the ability of the microscope to operate at cryogenic temperatures.

The microscope itself is built as a linear cage system that carries the wires, supports the optics, and otherwise joins all of the operational parts of the microscope together. This cage system is designed to fit into a long metal vacuum can and clamped closed, forming a vacuum-tight seal. It is engineered such that the microscope cage does not touch the sides of the vacuum can. The vacuum can is pumped out to ultra-high vacuum, typically below 10^{-6} Torr, to ensure that all nitrogen and other contaminants that could freeze are eliminated from the environment. Failing to do so could result in condensation on the optics or sample once the system is cooled to 4.2 Kelvin, contaminating the experiment.

Because of the thermal isolation that the thin layer of vacuum between the cage and the sides of the vacuum can provides, an exchange gas of approximately 10 Torr of helium is then added to the microscope. This is sufficiently low pressure that, once submerged in a liquid helium bath and cooled to 4.2 Kelvin, the helium exchange gas does not liquefy. However, it is a high enough pressure to facilitate thermal conduction between the cage and the metal can, allowing the sample and surrounding system to be brought into thermal equilibrium with the bath.

The metal vacuum can system is lowered into a vibration-isolated cryostat, which is then filled with liquid helium. Typically, as it is an order of magnitude less expensive by volume and has a much higher heat capacity, liquid nitrogen is used to pre-cool both the cryostat dewar and the microscope. After doing so, care is taken to remove all the liquid nitrogen from the dewar. Liquid nitrogen has a much higher heat capacity than liquid helium; any remaining liquid nitrogen would present a significant thermal mass for the liquid helium to cool, resulting in a large amount of wasted helium and defeating the purpose of pre-cooling.

3.1.4 Sample Positioning

One of the major benefits of the attoCube system is its inclusion of piezoelectric-based positioners. They consist of a stack of three stepper units, one for each of the x, y, and z axes, a separate 2-axis piezo scanner for fine position control, a heating element, and a silicon diode temperature sensor directly below the sample plate.

The steppers are based on a slip-stick design; when driven with a sawtooth wave, the linear rise is not rapid enough to overcome the coefficient of static friction so the sample plate moves together with the piezo movement. However, on the falling edge, the piezo contracts rapidly enough to overcome static friction and, much like a magician removing a tablecloth from below a stack of dishes, the sample plate does not move in the reverse direction with the piezo. In this fashion, the stepper units may position the sample over a range of 5 mm in each direction with only the two piezo wires needed to drive the unit. With the inclusion of a resistive strip encoder, it is possible to get repeatable positioning to within about 1 µm under fixed experimental conditions such as temperature.

The steppers and encoder readouts are controlled by a rack-mount unit which may be accessed via a USB driver interface. For this work, automation code was written in Python to interface with this driver so that it could be integrated with the rest of the code base.

The piezoelectric scanner unit is controlled with a bias voltage in the range 0 V–150 V, provided by another rack-mount controller. Communication with this controller occurs over a serial interface, which was also integrated into the Python automation code base.

3.1.5 Photon Counting

Everything prior to this point has involved establishing an *environment* with well known conditions for the quantum dots; a monochromator set to a known wavelength, a pump laser at a known power level, etc. However, nothing about the pieces described above involves an actual *measurement* of any property of the quantum dots or the

radiation that originates from them.

The measurement in this experiment is performed using an array of four superconducting nanowire single photon detectors (SNSPDs). Each detector is a superconducting nanowire that is biased just below its critical current density. When a photon is focused on these nanowires, it may be absorbed by one of them, breaking apart a Cooper pair, and forming a small hot-spot in the nanowire. This hot-spot is no longer superconducting and, accordingly, the current will divert around this resistive region. However, this increases the current density in the regions next to the hot spot beyond the critical value, creating a resistive bridge across the entire nanowire. As the nanowire has gone from zero resistance to a finite resistance, and there is a current flowing in it, a voltage is created across the nanowire. The nanowire will then thermalize rapidly with the substrate, regaining its superconducting state and eliminating the temporary potential. The result of this process is a voltage pulse that is amplified using a high electron mobility transistor (HEMT) and then fed via a transmission line to photon counting electronics, in this case a PicoQuant HydraHarp.

The detectors used in these experiments were measured to have approximately 55% detection efficiency at 1550 nm, a few hundred dark counts per second, and a dead time after photon detection of approximately 10 nanoseconds. This latter value is superseded by the HydraHarp's dead time of 80 nanoseconds after photon detection. Additionally, the system overall was capable of resolving the arrival time of photons to within 80 picoseconds.

The photon records are typically read out to the computer as a histogram of arrival times with respect to the electric sync signal from the Toptica laser. Because the radiative lifetime of the quantum dots is 1-2 ns, we may increase our signal-to-noise ratio (SNR) by only recording counts from part of this histogram.

Say we integrate for a period of time and record N total counts in the histogram. Call the histogram window duration t_w; at a 100 MHz repetition rate on the Toptica laser, this is 10 ns. If we expect $\langle n_d \rangle$ dark counts over the same integration time, our estimated signal is $N_s \approx N - \langle n_d \rangle$ and our signal to noise ratio is $\frac{N_s}{\langle n_d \rangle}$.

However, if our entire signal is contained in some time $t_s < t_w$, we may discard

detection events outside that time window. By assumption, all the counts outside this window are noise so, if we assume noise count arrivals are a stationary process, our noise is reduced by a factor of t_s/t_w while our signal is not reduced. The SNR is accordingly increased by a factor of t_w/t_s.

3.2 Optical Design

The only remaining part of the system to specify is the optical path of the microscope itself. Our goal here is to achieve as high a resolution as possible. A smaller spot size directly corresponds to fewer dots observed and thus a better chance of isolating a single quantum dot. Fundamentally, the main restriction on the spot size is the diffraction limit, described in Section 3.2.1. In principle, achieving the diffraction limit is not particularly difficult, even in the face of complications like chromatic aberration. However, there were a number of practical considerations introduced by this particular system that presented significant challenges. These centered on the access limitations imposed by the vacuum can and the disturbance to the optics introduced by maneuvering the microscope into the vacuum can, the vacuum can into the cryostat, and cooling everything to 4.2 Kelvin.

Notably, the only optical access to the vacuum can was through a single window at the top. There was no optical access at the bottom, near the sample and focusing lens. Further, the only imaging devices available for 1550 nm light were power meters and the SNSPDs. Both of these measure the intensity of light in a fiber, but no cameras were available to aid in aligning the confocal optics once the microscope was loaded into the vacuum can.

3.2.1 The Diffraction Limit

Light, as has been discussed, exhibits wave properties. As such, the ray-optics picture typically introduced when discussing lenses and mirrors is woefully incomplete in certain settings. Most important to the present discussion, it is impossible to focus waves to an arbitrarily small spot using a lens [30]. To see why this is true, it is

convenient to make the assumption that our imaging system is in the regime in which Fraunhofer diffraction holds. This is equivalent to viewing an aperture at infinity or, relevant to our consideration, examining the field at the focal plane of a positive lens [30].

Let $A(x, y, z)$ be the complex amplitude of a monochromatic scalar wave incident on a positive lens located at $z = 0$. Letting the focal distance of the lens be z_0, we are interested in the form of $A(x, y, z_0)$. If the conditions of Fraunhofer diffraction hold,

$$A(x, y, z_0) \propto \int\int_{\text{Pupil}} A(x', y', 0^+) e^{ik(x'x+y'y)} dx' dy' \tag{3.1}$$

where $A(x, y, 0^+)$ is the field at the output of the lens and $k = \frac{2\pi}{\lambda}$. Assuming the pupil is circular with radius R, we may convert this to polar coordinates:

$$A(r, \theta, z_0) \propto \int_0^{2\pi} \int_0^R A(r', \theta', 0^+) e^{ikrr' \cos(\theta-\theta')/z_0} r' dr' d\theta'. \tag{3.2}$$

Making the substitution

$$J_0(x) = \frac{1}{2\pi} \int_0^{2\pi} e^{ix\cos(a)} da \tag{3.3}$$

yields

$$A(r, z_0) \propto 2\pi \int_0^R A(r') J_0\left(\frac{krr'}{z}\right) r' dr'. \tag{3.4}$$

If we take the illuminating wave to have a constant intensity in the plane (i.e. illumination by a plane wave), we obtain the well-known Airy-disk solution:

$$A(r, z_0) \propto 2\pi \int_0^R J_0\left(\frac{krr'}{z}\right) r' dr' \propto \frac{J_1\left(\frac{kR}{z_0} r\right)}{\frac{kR}{z_0} r}. \tag{3.5}$$

If we make a small angle approximation, $R/z_0 \approx \sin(\theta)$. Further, denoting $k_0 = 2\pi/\lambda_0$ as the free-space wavenumber, we get

$$\frac{kR}{z_0} \approx k_0 n \sin(\theta) = k_0 \cdot \text{NA} \tag{3.6}$$

where n is the index of refraction of the environment and $\text{NA} \equiv n\sin(\theta)$ is the

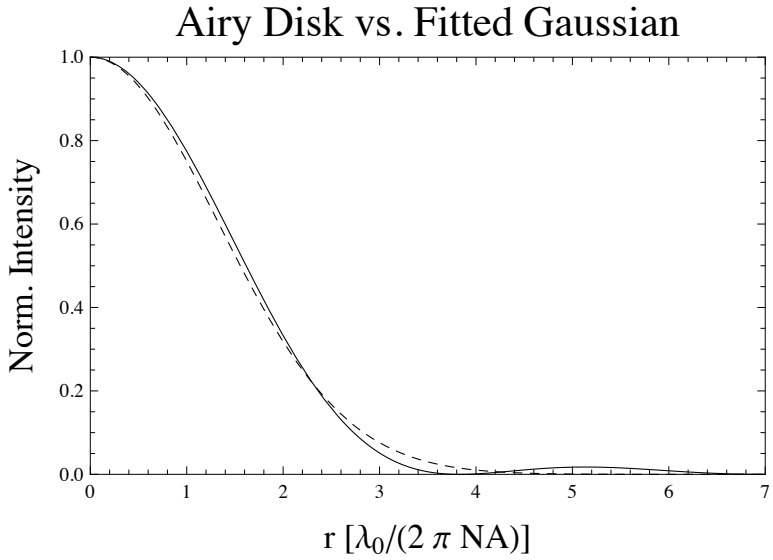

Figure 3-4: Comparison of an Airy Disk intensity $|2J_1(r)/r|^2$ and a Gaussian intensity $\left|e^{-x^2/2\sigma^2}\right|^2$ where $\sigma = 1.869$ was fitted to have the least mean square error over the visible plot range.

numerical aperture of the lens.

The zeros of the J_1 Bessel function are well established; the first nonzero root is at approximately 3.83. Rearranging, the first zero of the field profile in the focal plane is at $r = \frac{3.83}{k_0 \cdot \mathrm{NA}}$.

For our purposes, $A(r, z_0)$ is not quite the quantity of interest. We are primarily concerned with the number of photons per unit time, or the intensity of the radiation. This is proportional to the squared norm of the field amplitude, $I(r, z_0) = |A(r, z_0)|^2$. For reference, this is plotted in Figure 3-4.

The form of the Airy function is somewhat cumbersome mathematically. It is useful to find a Gaussian approximation that well-approximates the Airy function in the region of interest. The Gaussian amplitude function is proportional to $\exp\left(-\frac{x^2}{2\sigma^2}\right)$. Here, σ was calculated by numerical minimization of the integrated two-dimensional mean-squared error

$$\mathrm{MSE} = \int_0^{7.016} r \left(\left| e^{-\frac{x^2}{2\sigma^2}} \right|^2 - \left| 2\frac{J_1(k_0 r \mathrm{NA})}{k_0 r \mathrm{NA}} \right|^2 \right)^2 dr. \tag{3.7}$$

The upper integration bound of 7.016 corresponds to the second zero of the Airy disk; integration beyond this point did not yield a substantially different result. The best fit was found to be $\sigma = 1.869\frac{\lambda_0}{2\pi \mathrm{NA}}$; this Gaussian is also plotted in Figure 3-4.

A classical description of microscopy would now proceed with an analysis of the distinguishability of these functions centered at neighboring locations. However, the microscope under consideration has been designed as a scanning laser microscope whose inputs and outputs are single-mode fibers. As such, the image at a given configuration is completely described by a single scalar.

Changing the incident intensity profile above from a plane wave to a Gaussian beam (which is a reasonable approximation for the collimated image of a single mode fiber) does not appreciably change the resulting Airy disk profile. Instead, we now turn our attention to how confocal microscopy helps us decrease the radius of our imaged disk.

3.2.2 Confocal Microscopy

The argument for the use of confocal fluorescence microscopy is essentially founded on an assumption of a monotonic system response: if the pump laser intensity is lower at one spatial location than another, we expect the fluorescence from that point to be lower as well. Accordingly, the probability of receiving a photon from a given radius is a function of both the image of the pump laser and the image of the collection fiber tip. This combination is extremely straightforward: assuming the probability of excitation scales linearly with pump intensity, the overall probability of creation-and-collection of an excitonic photon is the product of the two individual intensity functions.

This combination of spots is especially important when we note that the x-axis of Figure 3-4 scales linearly with λ_0. That is, light of a shorter wavelength can be focused to a smaller spot. In particular here, our pump laser is half the wavelength of the emission we are interested in; its spot is plotted for comparison, along with the overall confocal response function, in Figure 3-5. Fitting a Gaussian to the confocal profile with the same method as before yields $\sigma_c = 0.854$.

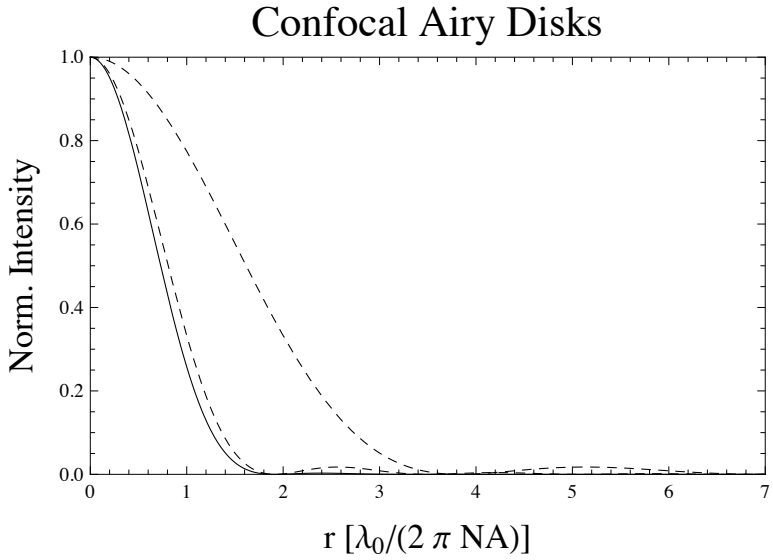

Figure 3-5: Comparison of the two individual Airy functions for $\lambda = \lambda_0$ and $\lambda = \frac{\lambda_0}{2}$ (the two dashed curves; $\frac{\lambda_0}{2}$ is the inner) with the overall confocal response function (the solid curve).

The first zero of the response function is found near $r = 1.92$; a reasonable rule of thumb is that the spot radius is approximately $\frac{\lambda_0}{\pi \mathrm{NA}}$. Plugging in a typical NA of 0.6 and our target λ_0 of 1550 nm, the nominal confocal spot radius is approximately 900 nm, corresponding to a spot area of 2.5 μm^2. However, this is the best case; due to the long length of the optical path in the microscope and the inability to directly measure the beam near the quantum dot sample while the microscope is sealed, it was necessary to validate the performance of the microscope in other ways.

3.2.3 Etched Mesas for Improved Isolation

In order to place an upper bound on the area of quantum dots being observed, an optical mask was designed and purchased to pattern the quantum dot samples. Specifically, the samples were patterned so that etching the samples would remove material (that is, quantum dots and the surrounding bulk lattice) from all areas except an array of circles. This left an array of mesas that still had quantum dots, while the rest of the substrate was no longer fluorescent at the wavelengths of interest.

The mask was designed so that a variety of mesa diameters and pitches (array

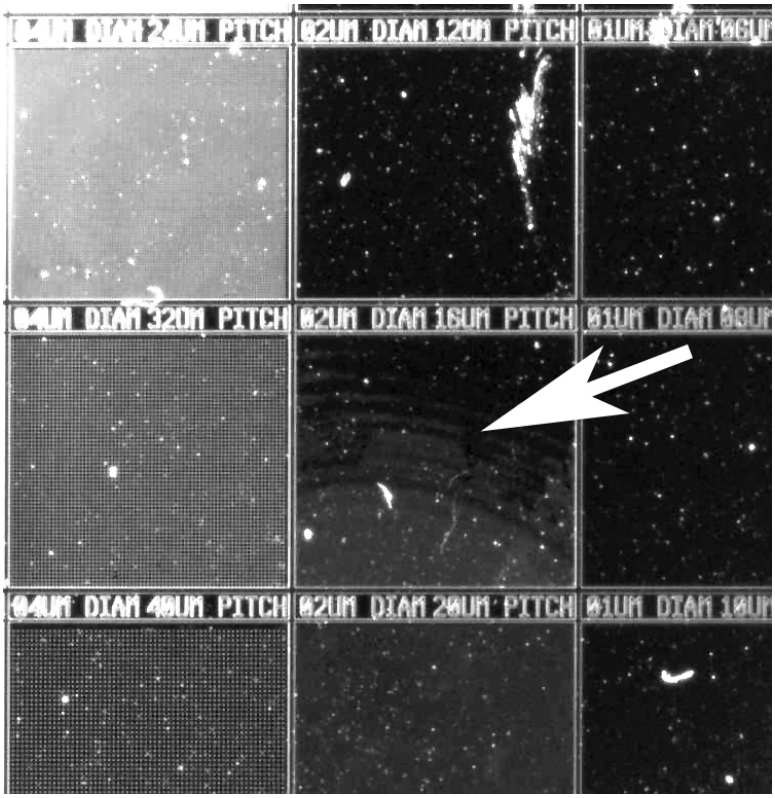

Figure 3-6: Photograph from a wide field microscope of a quantum dot sample etched with a variety of mesa diameters. The left column has mesas of 4 µm diameter, the middle column has mesas of µm diameter, and the right hand column would have containedm esas of 1 µm diameter, if any had resulted from the contact-mask process. The white arrow indicates where the 2 µm mesas fade away in the 16 µm pitch box; no 2 µm mesas exist in the 12 µm pitch box. There are no mesas in the 1µm boxes. Speckles over the sample are the result of the sample not being cleaned prior to the etching process; dust particles remained from the cleaving process, resulting in the speckles seen all over the image.

spacings) could be simultaneously patterned and etched. Specifically, mesa diameters 1 µm, 2 µm, 4 µm, and 8 µm were attempted, with pitches of $4\times$, $6\times$, $8\times$, and $10\times$ the mesa diameter. However, the contact lithography process was unable to resolve the 1 µm diameter mesas and only unreliably able to resolve the 2 µm mesas. See Figure 3-6 for a photograph of an etched sample.

In the end, enough 2 µm diameter mesas were successfully preserved through the etching process that we were able to make measurements on several quantum dot samples with these mesas. 2 µm diameter mesas have an area essentially equivalent to the ideal confocal spot size found in the preceding section. However, unlike the

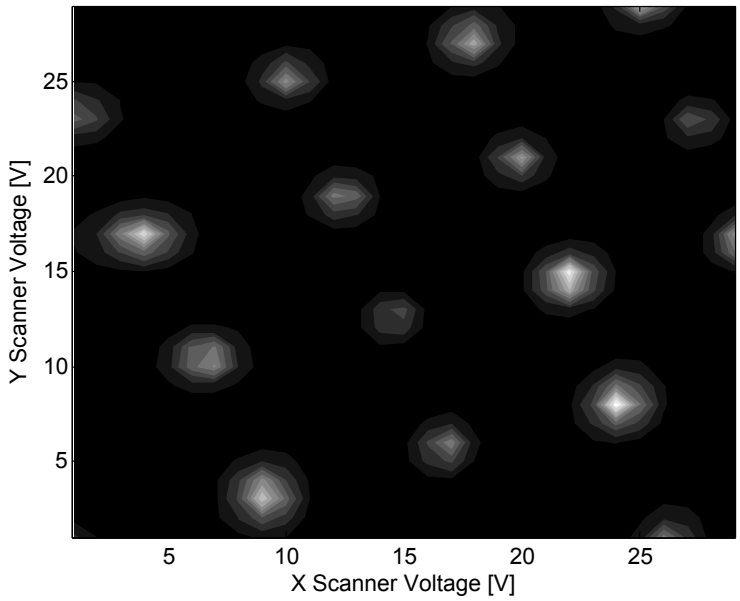

Figure 3-7: Raster scan of a sample with etched mesas. Gray scale indicates number of integrated counts. Taken with no spectral filtering.

optics, the etching process is permanent and does not need to be verified, making precise optical alignment slightly less crucial.

A raster scan of a quantum dot fluorescence from a sample with etched mesas is shown in Figure 3-7.

3.2.4 Etched Mesas for Validating Optical Performance

Originally, the decision to etch mesas into the quantum dot samples was motivated by an inability to isolate single quantum dots. However, these mesas also helped us uncover a flaw that had been lurking in the optical design.

The conventional way to verify scanning microscope performance is using some kind of reflection pattern, either an edge or, better, a patterned grating with a known structure. This allows you to confirm that the spot size of your microscope corresponds to your expectations. However, these measurements are based on reflection and therefore must be performed for each optical channel – pump and collection – separately. Reciprocity of the optical components makes this slightly easier; we may assume that the performance of a 1550 nm laser fed to the collection port is equiv-

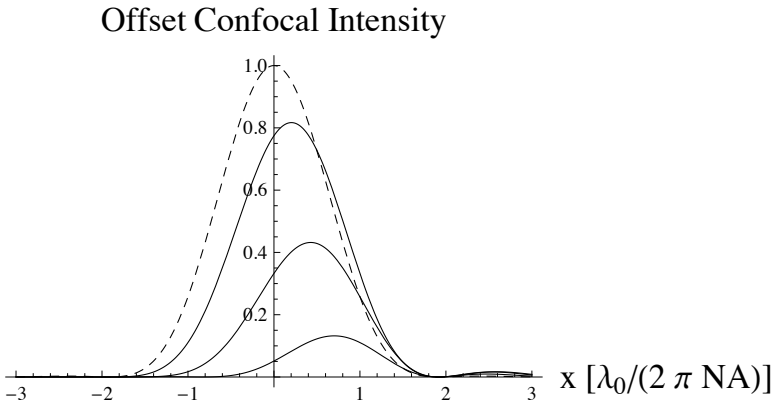

Figure 3-8: Illustration of the effect of misaligned spots in a confocal configuration. The dotted curve represents the aligned intensity, identical to the solid curve in Figure 3-5, and the three curves are offest by $\Delta x = 1, 2, 3$, with a larger offset corresponding to a smaller peak intensity.

alent to the performance of 1550 nm radiation in the opposing direction. However, the confocal spot size must be inferred by combining the individual spot patterns of each channel.

This is where the flaw in early optical designs lay: each channel was separately in focus and performing well, but they were not laterally aligned. As illustrated in Figure 3-8, this results both in a broadening of the spot and a decrease in overall efficiency because the dots from which we are trying to collect emission are not being efficiently stimulated.

Fortunately, having etched mesas with known sizes and patterns enabled us to detect and correct this error, as well as validate the performance of the microscope overall. Figure 3-9 shows the intensity profile obtained by raster scanning over a single mesa. The points represent total photon counts at that point and the surface is a fitted two-dimensional Gaussian with independent $\sigma_{\text{fit},x}$ and $\sigma_{\text{fit},y}$.

In order to characterize our microscope spot using these mesas, we need to predict the resulting image from a raster scan of a mesa of quantum dots. If we approximate our microscope spot as a two dimensional Gaussian, we expect this image to be the two-dimensional convolution of a Gaussian and a radial step function (i.e., a function that is constant for $r \leq R_{\text{mesa}}$ and zero else). However, this does not have a closed analytic form, so we instead proceed by iterative approximation: we estimate the

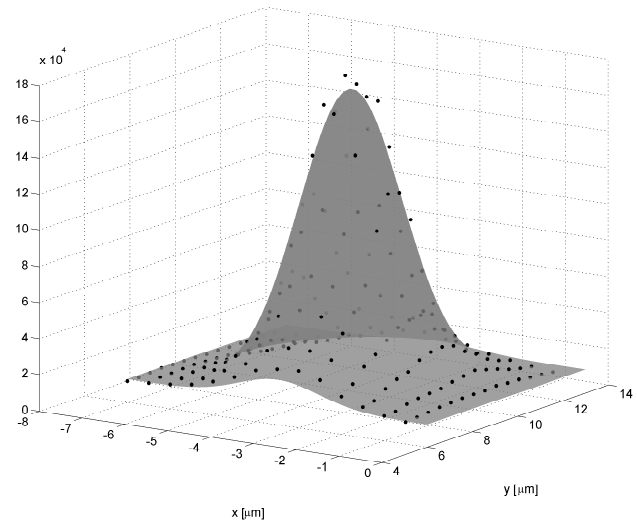

Figure 3-9: Measured fluorescence and fitted two-dimensional Gaussian of a 2 µm mesa on a quantum dot sample.

true Gaussian σ of the spot, numerically evaluate the two-dimensional convolution integral with a radial step of R_{mesa} µm, and then fit a two-dimensional Gaussian to the resulting structure. This gives us a $\tilde{\sigma}_{\text{fit}}(\sigma)$ that is intended to estimate σ_{fit} of the actual fitted data if the confocal Gaussian has parameter σ.

In order to invert this function, recovering σ_x and σ_y from $\sigma_{\text{fit},x}$ and $\sigma_{\text{fit},y}$, we fix the radius of the mesa, R_{mesa}, and calculate $\tilde{\sigma}_{\text{fit}}(\sigma)$ for a range of σ between 0.5 µm and 1.5 µm and fit a high-order polynomial to the results. Inverting this is significantly faster and more reliable than performing a direct nonlinear optimization of $\tilde{\sigma}_{\text{fit}}(\sigma)$, and the maximum error is of the order 10^{-7} µm, far below experimental error.

For the spot shown in in Figure 3-9, $\sigma_{\text{fit},x} = 0.955$ µm and $\sigma_{\text{fit},y} = 1.393$ µm. For $R_{\text{mesa}} = 1.0 \pm 0.2$ µm, the above process yields $\sigma_x = 0.76 \pm 0.10$ µm and $\sigma_y = 1.28 \pm 0.05$ µm, with a larger R_{mesa} corresponding to smaller σ_x and σ_y.

3.3 Summary

In this section, we have presented the experimental system as well as the design of the scanning confocal microscope used to characterize quantum dots. Importantly,

we have verified that we are able to obtain a small confocal spot size, and demonstrated etched mesas as a method of reducing the number of observed quantum dots. The quantum dot characterization results obtained with this system are presented in Chapter 4.

Chapter 4

Improving Quantum Dot Growth

The growth of quantum dot samples with the necessary properties for use in single photon sources is an active area of material science research. This is particularly true in the communications band; the first successes have only been reported in the last 7–8 years [19, 20, 21, 31]. For this work, we developed and began to refine our own epitaxy process based on successes in the literature.

Epitaxial quantum dots – the type used in this work – are produced by a process known as Stranski-Krastanov growth. In this growth mode, the lattice constant of the quantum dot material is larger than the lattice constant of the substrate, creating a compressive strain in the quantum dot layer during growth. Once the epitaxial layer reaches a certain thickness, known as the critical thickness, it becomes thermodynamically favorable for the material to form small islands – quantum dots – rather than remaining a single psuedomorphic layer [18, 22].

In this chapter, we discuss the organometallic vapor phase epitaxy (OMVPE) process we developed to grow quantum dots for single photon sources. The development of this process has occurred in parallel with the microscope and system work discussed in the previous chapter. Whereas feedback on different growth cycles is frequently a bottleneck in this type of work, integrating the growth and testing into a single project has resulted in more coordinated development and feedback.

In the next section, we give some background on the OMVPE process. We then present initial measurements of early quantum dots that motivated our developing

a new growth process. Finally, we present this new growth process and some initial spectroscopy results.

4.1 Organometallic Vapor Phase Epitaxy

OMVPE is an extremely versatile epitaxial growth process, allowing for the rapid growth of extremely pure semiconductor compounds and alloys. In particular, it is one of the most widely used growth methods for III-V semiconductor heterostructures. Crucial to the work in this thesis, OMVPE allows for precise control of epilayer thickness over a wide area in these heterostructures [32].

In the OMVPE reactor used in this work, 2-inch diameter substrates are mounted on a horizontal rotation plate in a low pressure (50 Torr) chamber. The samples are heated to a temperature between 500° Celsius and 700° Celsius. During the growth process, there is a constant flow of H_2 (diatomic hydrogen) gas from the top of the chamber, down onto the sample plate, and out a vent. This gas acts as a carrier for the constituents of the growth material. The reactor is designed so that that the H_2 flow is extremely uniform in the chamber to ensure consistent growth across the surface of the substrate. To further enhance this uniformity, the sample plate is rotated at 500 RPM.

As the name of the process implies, the semiconductor elements are carried by organic molecules, known as precursors. The group-III elements are transported in the form of an alkyl-metal gas; for Indium, we used trimethylindium. The group-V elements are contained in hydride molecules such as arsine (AsH_3) or phosphine (PH_3).

During growth, these precursors are transported by the H_2 gas to the hot surface of the substrate, where they undergo pyrolysis[1], forming a boundary layer between the substrate and the bulk stream. In this boundary layer, the crystal constituents become free cations (group-III elements) and anions (group-V elements). These ions adsorb to the substrate, resulting in layer-by-layer growth at the atomic level. The

[1]Temperature-induced decomposition of organic molecules

growth rate and properties of the resulting crystal are entirely dependent on the properties of the boundary layer and the substrate [32, 33].

4.1.1 Group-V Exchange

There is one feature of OMVPE growth that should be highlighted for its importance to the quantum dot growth process we developed: when growing a III-V semiconductor alloy with multiple group-V elements (e.g., $InAs_xP_{1-x}$, where subscripts indicate alloy composition) or growing a semiconductor compound with a different group-V element than the substrate (e.g., InAs on an InP substrate, as in this work) there is a significant exchange and diffusion effect for the anions that is difficult to model or quantify.

The strength of the anion exchange has several root causes: the incomplete pyrolysis of the anion source molecules, the large ratio of group-V precursor atoms to group-III precursor atoms[2], and the high volatility of the anions. Due to this exchange, the boundary of InAs and InP cannot typically be regarded as abrupt; there is a certain amount of alloying that occurs [33].

4.2 Early Quantum Dot Results

When this thesis work was started, some initial growth tests of quantum dots had already occurred. Early measurements and tests of the microscope were performed using these samples. The results of these initial measurements – we were unable to isolate sharp spectrographic lines characteristic of the desired electronic confinement – drove us to develop the OMVPE process described later in this chapter. In this section, we discuss these early quantum dots and some representative characterization results for them.

[2]This is known as the V-III ratio; its value during growth is typically anywhere from 5-200

4.2.1 Early Quantum Dot Growth Process

It was initially believed that the group-V exchange reaction discussed earlier would limit the ability to control growth parameters such as quantum dot density independently from the alloying at the surface, making it more difficult to understand the growth process and optimize the quantum dot films. Additionally, it is possible that this alloying would reduce the electronic confinement in the quantum dots. Referring back to the simple electronic model from Chapter 2, in a structure where the quantum dots are surrounded by a slowly-varying alloy $InAs_xP_{1-x}$, we would expect the electron effective mass to change gradually. This slow variation is in contrast to the rapid effective-mass barrier assumed in that model. In the slowly-varying case, we would expect the electronic confinement to be much weaker, potentially allowing a spectrum of states rather than just isolated single states.

To prevent this alloying, a thick buffer layer composed of a quaternary semiconductor with As as its group-V element, $Al_xGa_yIn_{1-x-y}As$, was first grown on the InP substrate. Quaternary semiconductors are convenient as they have two free parameters in their composition, allowing one to tune both the lattice constant to match that of the substrate while also adjusting the size of the band gap. Matching the lattice constant of the buffer layer to that of InP maintained the lattice mismatch between InAs and the substrate necessary for Stranski-Krastanov growth. The band gap was tuned to be around 1 eV, far from 0.78 eV, which is the target energy for the lowest excited state in the InAs quantum dots.

After a capping layer of AlGaInAs was grown over the quantum dots, a second layer of dots was grown on the outer surface. While being optically inactive due to interactions with surface states of the crystal, their size and density give a rough estimate of what to expect for the optically active interior quantum dots. These surface dots were characterized using atomic force microscopy (AFM) and yielded information about density, height, and lateral size of the quantum dots. A typical AFM scan is shown in Figure 4-1.

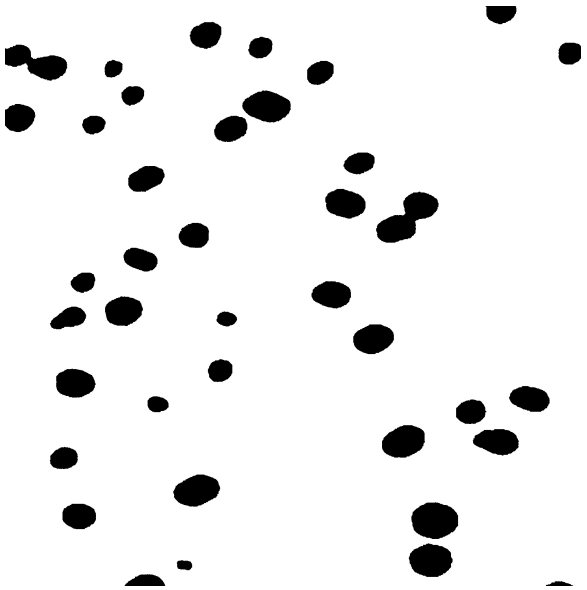

Figure 4-1: 1 µm×1 µm AFM Scan of the surface of quantum dot sample 10-980. The three-dimensional AFM was converted to this two-dimensional figure by a height threshold applied at 2 nm. The minimum quantum dot height was 2.2 nm, the maximum was 11.6 nm, and the average was 7.2 nm.

4.2.2 Initial Quantum Dot Fluorescence Results

We present here the results of measurements on two different samples, 10-980 and 10-981, that are representative of our early quantum dots. The AFM scan of sample 10-980 in Figure 4-1 shows that the quantum dots tend to be consistently oblong, with essentially parallel major axes. The AFM measurements of Sample 10-980 found a density of about 39 μm^{-2}, an average quantum dot height of 7.2 nm, an average major axis of 62 nm, and an average minor axis of 39 nm. For sample 10-981, the AFM measurements showed an average density of about 0.5 μm^{-2}, an average dot height of 3.4 nm, an average major axis of 43 nm, and an average minor axis of 33 nm.

Due to the density of dots on sample 10-980, it was one of the samples patterned with mesas prior to measurement. The reported results are from experiments performed on 2 µm diameter mesas. Figure 4-2 shows a fluorescence raster scan of the mesas as well as a spectral scan demonstrating a wide peak centered near 1540 nm. The dot density on sample 10-981 was deemed to be low enough that we did not pattern it with any mesas.

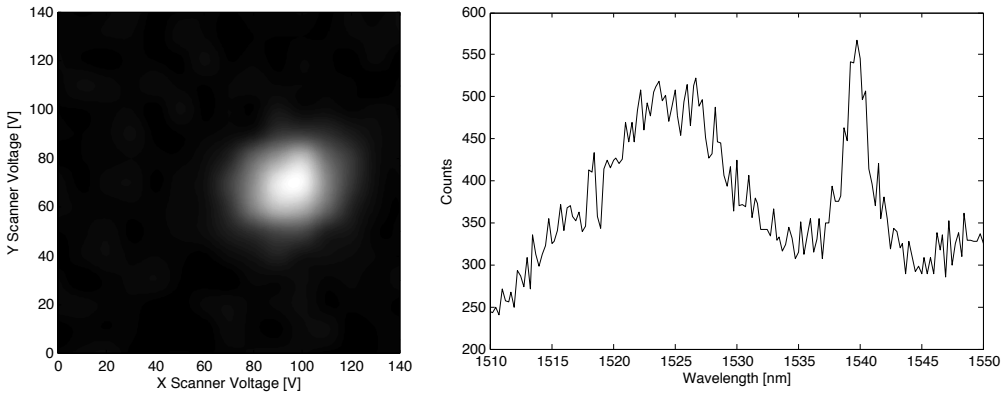

(a) Raster Scan (b) Spectrum

Figure 4-2: Fluorescence Results for sample 10-980, acquired with the sample at 4.2 Kelvin. The raster scan was taken with the monochromator in the optical path, tuned to a center wavelength of 1525 nm and a bandwith of 0.5 nm. The spectrum was taken with the scanner positioned at (90 V, 70 V), which maximized the photon count rate. The spectrum is taken in steps of 0.25 nm with the monochromator window set to 0.25 nm, integrating for 2.5 seconds at each point.

For both samples, we isolated a small enough area and spectral region that, if the quantum dots were providing the desired quantum confinement, we should have been able to see sharp spectral lines. For sample 10-980, we measured radiation from a single mesa that had an area of 3 μm^2, or 80 expected dots. These early dots were measured to have an ensemble spectrum whose center wavelength was red detuned from 1550 nm; in the case of 10-980, the ensemble spectrum was centered near 1640 nm. Similarly, on sample 10-981, we were looking at a low density of dots over a small area, and could see well defined features.

Thus, for both samples 10-980 and 10-981, we expected few enough dots that we should have seen a forest of spectral lines. However, we did not see such spectra for either sample. The distribution of a large collection of dots should be approximately Gaussian; see, for example, the spectra presented in Figure 4-4. However, the spectra in Figures 4-2 and 4-3 look more Lorentzian than Gaussian, which is characteristic of small quantum well structures with a spectrum of energy states. Our conclusion from these experiments, and similar ones performed on other samples grown by this method, was that we needed a new method of growth that would result in smaller

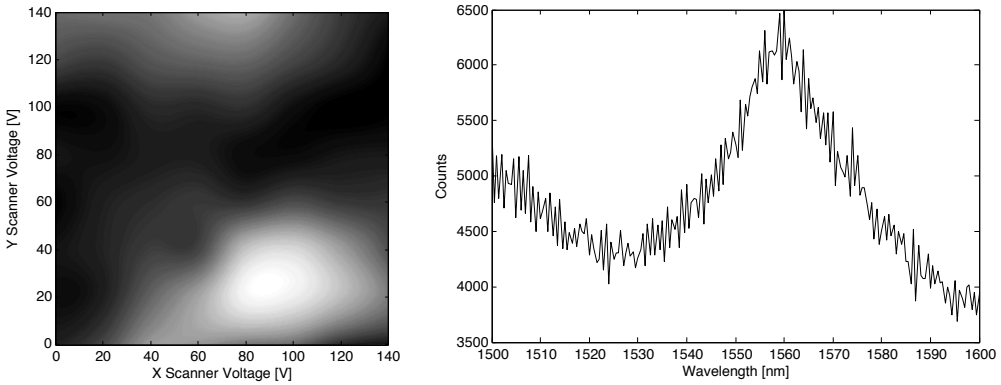

(a) Raster Scan (b) Spectrum

Figure 4-3: Fluorescence results for sample 10-981, acquired with the sample at 4.2 Kelvin. The raster scan was taken with a bandpass filter installed in the optical path so that only radiation in the band 1530 nm – 1570 nm is visible. The spectrum was acquired with the scanner set to (90 V, 30 V), which maximized the photon count rate. The spectrum was acquired in steps of 0.25 nm, with the monochromator window set to 0.25 nm, integrating for 40 seconds at each point.

dots with better quantum confinement: our early dots were behaving too much like small quantum wells.

4.3 Double Cap Method

A review of the literature on quantum dot growth revealed that several groups who have had success growing these dots for single photon applications were applying a double-cap method that took advantage of, rather than avoided, the group-V exchange reaction [34, 35, 36]. In this process, a sample of quantum dots is grown under normal conditions for Stranski-Krastanov growth until just before the capping layer on top of the dots is deposited. Typically, this capping layer is deposited as one continuous growth. However, in the double-cap method, the growth of this capping layer is interrupted after several nanometers of material is deposited. This initial capping layer covers the base of the dots, but leaves the tops of the dots exposed. Then, the group-III precursor, arsine, is blocked and an H_2 gas carrying only the group-V precursor, phosphine, is flowed over the sample for a relatively long time, usually up to two minutes (whereas the growth of the dot layer takes only 6-10 seconds). Due to

the group-V exchange, this second step acts as an etch, converting the exposed tops of the dots from InAs into InP. Measurements in the literature suggest [34, 36] that this process creates a sharp interface between the InAs dot and the InP capping layer. Once this etching process has taken place, the rest of the capping layer is deposited in the usual fashion.

Informed by the successes in the literature, we have adopted this process and have begun tuning it to work in our reactor. OMVPE processes, especially those involving group-V exchange, are notoriously sensitive to reactor design as even slight differences in flow consistency and uniformity can drastically modify the parameters needed to obtain a particular epitaxial result [33, 37]. In the rest of this section, we present an example of the specific growth process, highlight the variables we have chosen to modify, and present initial fluorescence results for the resulting samples.

4.3.1 Growth Process Overview

Here is an example growth process for a sample of double-capped quantum dots. The actual growth steps are in bold-face, while comments on these steps are in normal typeface.

1. **Load InP wafer into reactor, heat to 650° Celsius to desorb oxidized layer from surface of wafer.** This step was left unchanged in all growth runs.

2. **Cool to 550° Celsius and grow 250 nm of intrinsic InP as a pure buffer layer. Growth is at a V/III ratio of 125.** This step was left unchanged in all growth runs.

3. **Cool to 525° Celsius and grow 2.2→3.0 monolayers (MLs) of InAs at a V/III ratio of 5→20.** Here, both the V/III ratio and the thickness of the quantum dot layer were varied. The V/III ratio affects the group-V exchange process during growth, as well as the size and density of the quantum dots produced. The thickness of the layer affects mostly the size and density of the dots, with a thicker InAs layer producing more, smaller dots.

4. **Anneal dots under arsine for 20 seconds.** This step was varied to shorter times; we was found that shorter arsine anneals led to samples without quantum dot fluorescence.

5. **Grow first InP capping layer at a V/III ratio of 125.** The thickness of this layer was tested at 1 nm and 2 nm.

6. **Stop flow of trimethylindium, anneal dots under flow of phosphine for 120 seconds.** Shorter anneal times were tested, but found to reduce the effects of the double-capping process without clear benefit.

7. **Grow second InP capping layer at a V/III ratio of 125.** We kept the total cap thickness at 20 nm, varying this layer's thickness to accommodate the thickness of the first InP capping layer.

8. **Cool down sample and remove from chamber.**

The most important parameter was the amount of InAs deposited. Although we varied other parameters, it had the most effect by far, and is the basis for the following results discussion.

4.3.2 Fluorescence Results

After a few iterations between growth and testing, we were able to get quantum dot spectra centered around 1550 nm – 1600 nm as measured at room temperature. At this point, we fixed all of the parameters except one, the InAs thickness, and performed a series of three test runs; these were at InAs layer thicknesses of 2.2 ML, 2.5 ML and 3.0 ML. In alternating runs, we also grew control samples that were identical to the double-capped samples except that we omitted the growth interruption and phosphine anneal. The results from these six samples are presented here.

First, in Figure 4-4, we present wide-area room temperature measurements of the fluorescence spectrum. These were performed by a collaborator using a 3 µm-grating based spectrometer. While the vertical units are arbitrary, the scale is consistent

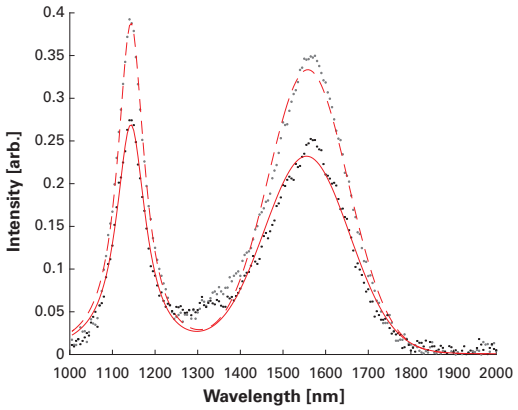

(a) 2.2 ML Growth Runs

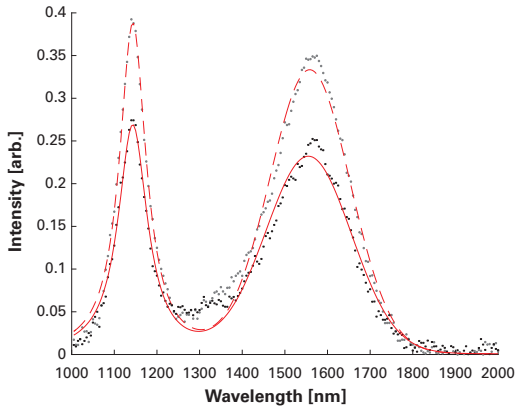

(b) 2.5 ML Growth Runs

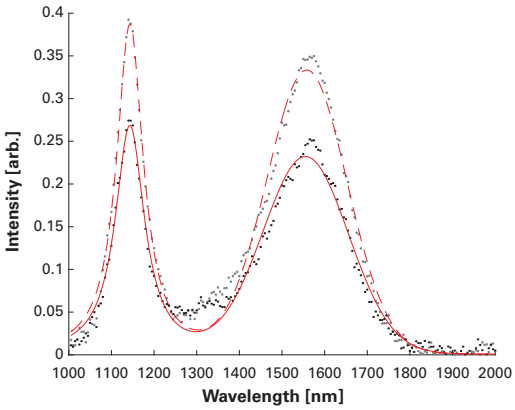

(c) 3.0 ML Growth Runs

Figure 4-4: Room temperature fluorescence measurements comparing a double-capped sample (black circles, solid line for fit) to a control sample (gray circles, dotted line for fit) grown identically, except for omitting the growth interruption and 120 second anneal under phosphine. The fit function is the sum of a Lorentzian for the quantum well, centered near 1150 nm, and a Gaussian for the quantum dot spectrum, centered near 1550 nm. Fits were also run with Voigt profiles to no significant benefit.

Fit values for the quantum dot Gaussian are listed in the table below. The quantum well, other than varying in magnitude, did not appreciably change. μ refers to the mean of the Gaussian, σ to the standard deviation.

InAs Thickness [ML]	Control μ	Double-Cap μ	Control σ	Double-Cap σ
2.2	1590.9	1557.1	81.7	100.8
2.5	1558.6	1555.7	94.2	100.6
3.0	1602.4	1571	80.6	94.7

between the panels of Figure 4-4. These spectra were fit with the sum of a single Lorentzian, centered near 1150 nm and a single Gaussian, centered near 1550 nm, with good fits obtained. The Lorentzian corresponds to the expected spectrum of the wetting layer, a thin layer left behind by Stranski-Krastanov growth that forms a quantum well. The Gaussian corresponds to the expected ensemble spectrum of the quantum dots. These were also fit with the sum of two Voigt profiles[3] with no relevant difference; the Gaussian term of the first peak and the Lorentzian term of the second were consistently near zero.

The Table in Figure 4-4 provides fit parameters, which show that the effects of the double-capping process on the ensemble spectrum seem to have been most significant for the 2.2 ML and 3.0 ML samples, with almost no change occurring for the 2.5 ML sample.

Next, in Figure 4-5, we present measurements made on four of these samples – the two 2.2 ML samples and the two 2.5 ML samples – at 4.2 Kelvin using the confocal microscope. The measurement conditions were carefully maintained across the measurement of all four samples, and the data was taken in a single cool-down of the microscope. As such, the ordinate, photon counts, is a calibrated value throughout the five plots.

The results in Figure 4-5 show a change in spectral shape due to the double-capping process, but do not suggest that these dots have the sharp spectral features we would like. Further work on refining the OMVPE growth process will undoubtedly be necessary. Potential avenues for this refinement are discussed in Chapter 5.

[3] A Voigt profile is the convolution of a Lorentzian and a Gaussian. These are typically used to fit spectral lines (a Lorentzian) that have been broadened either by temperature or by the measurement process (resulting in convolution with a Gaussian).

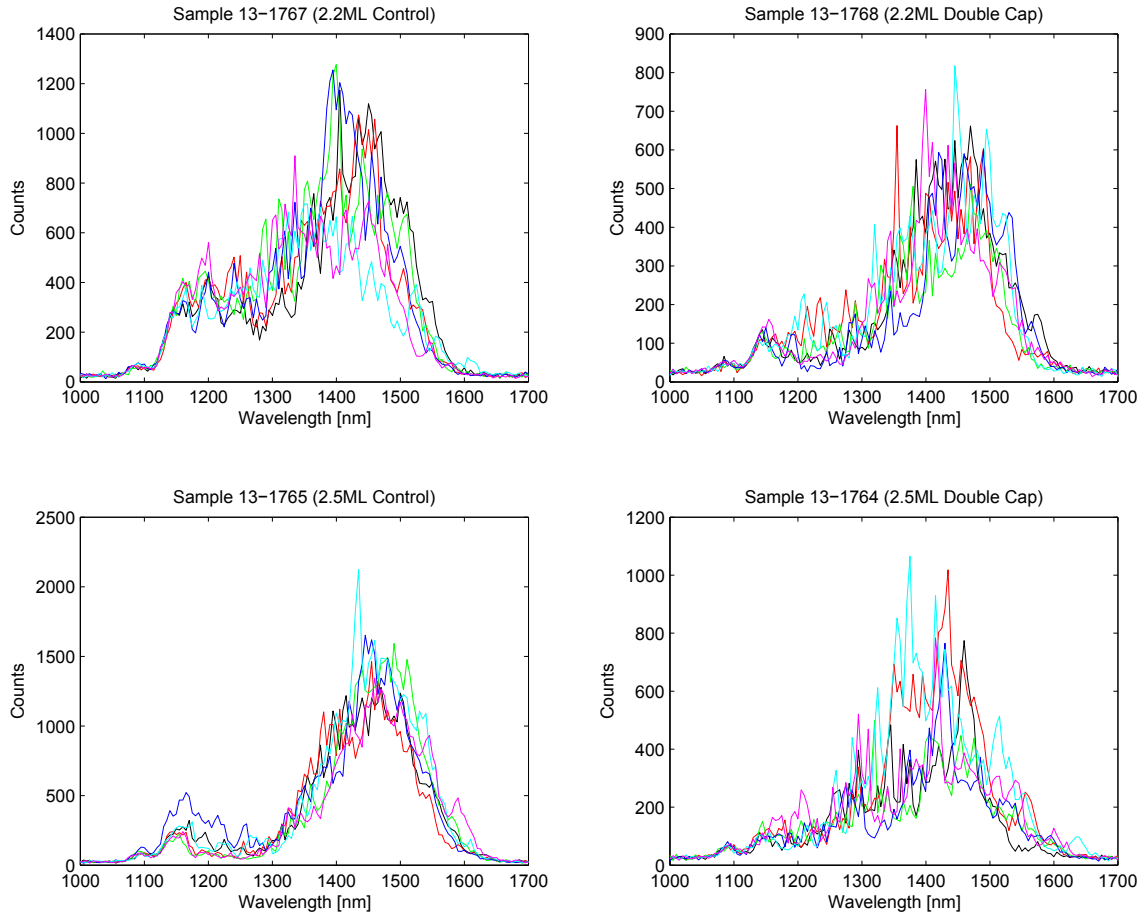

(a) Spectra from the four samples measured at 4.2 Kelvin. Different lines indicate scans taken at different positions on the sample; color is arbitrary.

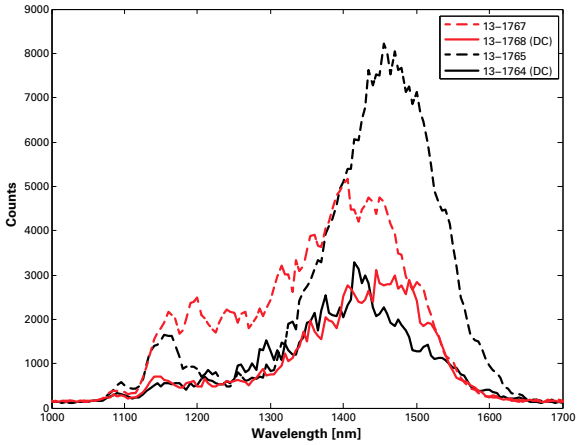

(b) Averages of the spectra in (a), plotted together for comparison. Control samples are shown with dotted lines, double-capped samples with solid lines. Red lines indicate a 2.2ML InAs layer; black a 2.5 ML InAs layer.

Figure 4-5: Collection of cryogenic spectra acquired for samples 13-1767 and 13-1768.

Chapter 5

Conclusions and Future Work

In this thesis, we have presented work in two areas toward the realization of a single photon source in the C-Band using semiconductor quantum dots. We demonstrated the successful design, construction, and validation of a scanning-laser confocal microscope operating at cryogenic temperatures. This work interacted directly with the second avenue of progress, suggesting the need for and directly aiding the the development of an improved growth process for these quantum dots, with the confocal microscope providing closely coupled feedback for evaluating the quantum dot growth process. Preliminary results from this new process suggest that more work needs to be done before a single photon source can be realized. At this point, we have identified three main directions for that future work, as detailed below.

5.1 Improvements to the OMVPE Process

There are several potential improvements to be made to the OMVPE process. One option is to proceed as we have been, staking out variables to test against control samples and seeking correlations with the observed spectra. This is a reasonable approach, but hindered by the huge search space and significant testing required to provide detailed feedback.

More exciting is the plan to combine the ideas of the old and new quantum dot growth processes. It is possible that the vertical alloying effect between the InAs dots

and the InP is making it difficult to achieve electronic confinement. The next step would be to perform the first half of the growth as we did originally, with an AlGaInAs buffer layer between the InP substrate and the quantum dots. Then, after depositing the quantum dots, the growth is switched to InP, making use of the group-V exchange and double-capping method to pare down the size of the quantum dots.

This method would allow us to ensure sharp edges at both the top and bottom interfaces of the quantum dots. At the bottom, this improvement would result from the lack of group-V exchange, whereas on top it would result from the double-capping process. As the vertical direction is the primary axis of confinement in these dots, this change would hopefully improve the quantum confinement.

5.2 Improved Isolation of the Quantum Dots

In the interest of isolating single dots, we may again make use of the patterned mesas. However, if we wish to isolate even smaller areas, there are several ways to proceed. The one with the fastest turnaround is the method used in [18] to grow micro-pillar cavities: Sapphire dust is scattered on the sample and used as a mask for vertical etching. Because of the tiny size of the particles, van der Waals forces are sufficient to hold them in place through the etch, creating micro-pillars. Alternatively, we could try a more controlled approach, such as using focused ion beam lithography to etch mesas of much smaller diameter than we achieved previously with contact lithography.

5.3 Integration into Photonic Crystal Cavities

Finally, we are currently collaborating with another group to integrate these quantum dots into photonic crystal cavities. Photonic crystals are periodic dielectric structures that are carefully designed so that there is a photonic band gap of energies that are prohibited. The origin of this effect is precisely analogous to the breaking of continuous translational symmetry through discrete structural periodicities discussed for electrons in Chapter 2. In effect, the dielectric structure provides a Hamiltonian

whose the potential is proportional to the inverse of the dielectric constant [38].

One of the most successful implementations of photonic crystals has been planar micro-cavities. It is this type of photonic crystal into which we want to integrate our quantum dots. They work by creating a photonic crystal with a band gap for light propagating within the substrate around the desired resonant frequency. Then, a defect is created wherein a localized state is created, much like a bound state in a quantum well. Because these states are so well confined, extremely high cavity resonances can be achieved experimentally, leading to enhanced interaction between the dipole transition and the electromagnetic field [38].

Integration of quantum dots into these cavities is promising for several reasons. First, the cavities are extremely sensitive to quantum dot placement *within* the cavity, so they enhance our ability to address a single quantum dot [39]. Further, once a quantum dot is aligned with a cavity, it is possible to obtain strong coupling between the dipole transition in the dot and the resonant electric field mode. In this case, which occurs when the ratio of the quality factor to the mode volume is large, the Purcell effect appears, decreasing the radiative lifetime of the transition and thus enabling higher-rate single photon production.

Finally, the cavities can be fabricated so as to aid collection of the emitted radiation into a usable spatial mode, enhancing the efficiency of the measurement being made and increasing the probability that a photon will be collected when the source is triggered.

Bibliography

[1] A. Einstein, "ber einen die erzeugung und verwandlung des lichtes betreffenden heuristischen gesichtspunkt," *Annalen der Physik*, vol. 322, no. 6, pp. 132–148, 1905.

[2] P. A. M. Dirac, "The quantum theory of the emission and absorption of radiation," *Proceedings of the Royal Society of London. Series A*, vol. 114, no. 767, pp. 243–265, 1927.

[3] P. A. M. Dirac, "The quantum theory of dispersion," *Proceedings of the Royal Society of London. Series A*, vol. 114, no. 769, pp. 710–728, 1927.

[4] W. Heisenberg and W. Pauli, "Zur quantentheorie der wellenfelder. ii," *Zeitschrift fr Physik*, vol. 59, no. 3-4, pp. 168–190, 1930.

[5] E. Fermi, "Quantum theory of radiation," *Rev. Mod. Phys.*, vol. 4, pp. 87–132, Jan 1932.

[6] M. Nielsen and I. Chuang, *Quantum Computation and Quantum Information: 10th Anniversary Edition*. Cambridge University Press, 2010.

[7] J. J. Sakurai, *Modern quantum mechanics*. Addison Wesley Publishing Company Incorporated, 2011.

[8] C. H. Bennett, G. Brassard, *et al.*, "Quantum cryptography: Public key distribution and coin tossing," in *Proceedings of IEEE International Conference on Computers, Systems and Signal Processing*, vol. 175, Bangalore, India, 1984.

[9] L. Lydersen, C. Wiechers, C. Wittmann, D. Elser, J. Skaar, and V. Makarov, "Hacking commercial quantum cryptography systems by tailored bright illumination," *Nature photonics*, vol. 4, no. 10, pp. 686–689, 2010.

[10] L. Lydersen, J. Skaar, and V. Makarov, "Tailored bright illumination attack on distributed-phase-reference protocols," *Journal of Modern Optics*, vol. 58, no. 8, pp. 680–685, 2011.

[11] I. Gerhardt, Q. Liu, A. Lamas-Linares, J. Skaar, C. Kurtsiefer, and V. Makarov, "Full-field implementation of a perfect eavesdropper on a quantum cryptography system," *Nature communications*, vol. 2, p. 349, 2011.

[12] C. M. Santori, D. Fattal, and Y. Yamamoto, *Single-Photon Devices and Applications*. Verlag: Wiley-VCH, 2010.

[13] C. M. Santori, D. Fattal, J. Vučković, G. S. Solomon, and Y. Yamamoto, "Generation of single photons and correlated photon pairs using InAs quantum dots," *Fortschritte der Physik*, vol. 52, pp. 1180–1188, Nov. 2004.

[14] C. M. Santori, D. Fattal, J. Vučković, G. S. Solomon, and Y. Yamamoto, "Indistinguishable photons from a single-photon device," *Nature*, vol. 419, pp. 594–597, Oct. 2002.

[15] Y. Yamamoto, "Quantum communication and information processing with quantum dots," *Quantum Information Processing*, vol. 5, pp. 299–311, Aug. 2006.

[16] M. A. Broome, A. Fedrizzi, S. Rahimi-Keshari, J. Dove, S. Aaronson, T. C. Ralph, and A. G. White, "Photonic boson sampling in a tunable circuit," *Science*, vol. 339, no. 6121, pp. 794–798, 2013.

[17] K. T. Shimizu, R. G. Neuhauser, C. A. Leatherdale, S. A. Empedocles, W. K. Woo, and M. G. Bawendi, "Blinking statistics in single semiconductor nanocrystal quantum dots," *Phys. Rev. B*, vol. 63, p. 205316, May 2001.

[18] C. M. Santori, *Generation of Nonclassical Light Using Semiconductor Quantum Dots*. PhD thesis, Stanford, 2003.

[19] M. D. Birowosuto, H. Sumikura, S. Matsuo, H. Taniyama, P. J. van Veldhoven, R. Nötzel, and M. Notomi, "Fast purcell-enhanced single photon source in 1,550-nm telecom band from a resonant quantum dot-cavity coupling," *Scientific reports*, vol. 2, 2012.

[20] K. Takemoto, S. Hirose, M. Takatsu, N. Yokoyama, Y. Sakuma, T. Usuki, T. Miyazawa, and Y. Arakawa, "Telecom single-photon source with horn structure," *physica status solidi (c)*, vol. 5, no. 9, pp. 2699–2703, 2008.

[21] K. Takemoto, Y. Nambu, T. Miyazawa, K. Wakui, S. Hirose, T. Usuki, M. Takatsu, N. Yokoyama, K. Yoshino, A. Tomita, S. Yorozu, Y. Sakuma, and Y. Arakawa, "Transmission experiment of quantum keys over 50 km using high-performance quantum-dot single-photon source at 1.5 μm wavelength," *Applied Physics Express*, vol. 3, no. 9, p. 092802, 2010.

[22] V. A. Shchukin, N. N. Ledentsov, P. S. Kop'ev, and D. Bimberg, "Spontaneous ordering of arrays of coherent strained islands," *Phys. Rev. Lett.*, vol. 75, pp. 2968–2971, Oct 1995.

[23] Y. Saad, *Numerical Methods for Large Eigenvalue Problems*. Classics in Applied Mathematics, Society for Industrial and Applied Mathematics, 2011.

[24] D. J. Griffiths, *Introduction to quantum mechanics*. Pearson Prentice Hall, 2005.

[25] P. Morse and H. Feshbach, *Methods of theoretical physics, Volume 1.* International series in pure and applied physics, McGraw-Hill, 1953.

[26] N. Ashcroft and N. Mermin, *Solid state physics.* Science: Physics, Saunders College, 1976.

[27] O. Gywat, H. Krenner, and J. Berezovsky, *Spins in Optically Active Quantum Dots.* Wiley, 2009.

[28] E. Biolatti, I. D'Amico, P. Zanardi, and F. Rossi, "Electro-optical properties of semiconductor quantum dots: Application to quantum information processing," *Physical Review B*, vol. 65, p. 075305, 2002.

[29] J. Jackson, *Classical Electrodynamics.* New York: John Wiley & Sons, 2nd ed., 1975.

[30] M. Born and E. Wolf, *Principles of Optics: Electromagnetic Theory of Propagation, Interference and Diffraction of Light.* Cambridge University Press, 1999.

[31] T. Miyazawa, K. Takemoto, Y. Sakuma, S. Hirose, T. Usuki, N. Yokoyama, M. Takatsu, and Y. Arakawa, "Single-photon generation in the 1.55-μm optical-fiber band from an inas/inp quantum dot," *Japanese Journal of Applied Physics*, vol. 44, no. 20, pp. L620–L622, 2005.

[32] C. A. Wang, "A new organometallic vapor phase epitaxy reactor for highly uniform epitaxy," *The Lincoln Laboratory Journal*, vol. 3, no. 1, pp. 3–22, 1990.

[33] G. Stringfellow, *Organometallic Vapor-Phase Epitaxy: Theory and Practice.* Elsevier Science, 1999.

[34] Y. Sakuma, M. Takeguchi, K. Takemoto, S. Hirose, T. Usuki, and N. Yokoyama, "Role of thin inp cap layer and anion exchange reaction on structural and optical properties of inas quantum dots on inp (001)," *J. Vac. Sci. Technol. B*, vol. 23, no. 4, pp. 1741–1746, 2005.

[35] Y. Sakuma, K. Takemoto, S. Hirose, T. Usuki, and N. Yokoyama, "Controlling emission wavelength from inas self-assembled quantum dots on inp (001) during mocvd," *Physica E: Low-dimensional Systems and Nanostructures*, vol. 26, no. 1 - 4, pp. 81 – 85, 2005. International Conference on Quantum Dots.

[36] Y. Akanuma, I. Yamakawa, Y. Sakuma, T. Usuki, and A. Nakamura, "Scanning tunneling microscopy study of interfacial structure of inas quantum dots on inp(001) grown by a double-cap method," *Applied Physics Letters*, vol. 90, no. 9, p. 093112, 2007.

[37] C. Wang. personal correspondence, 2011.

[38] J. Joannopoulos, S. Johnson, J. Winn, and R. Meade, *Photonic Crystals: Molding the Flow of Light (Second Edition).* Princeton University Press, 2011.

[39] D. Englund, D. Fattal, E. Waks, G. Solomon, B. Zhang, T. Nakaoka, Y. Arakawa, Y. Yamamoto, and J. Vučković, "Controlling the spontaneous emission rate of single quantum dots in a two-dimensional photonic crystal," *Phys. Rev. Lett.*, vol. 95, p. 013904, Jul 2005.